Neotethyan Subduction Ignited the Iran Arc and Backarc Differently

H. Shafaii Moghadam[1,2,3,4] [iD], **Q. L. Li[1]** [iD], **X. H. Li[1]** [iD], **R. J. Stern[5]** [iD], **G. Levresse[6]** [iD], **J. F. Santos[7]** [iD], **M. Lopez Martinez[8]** [iD], **M. N. Ducea[9,10]** [iD], **G. Ghorbani[2]**, and **A. Hassannezhad[2]**

[1]State Key Laboratory of Lithospheric Evolution, Institute of Geology and Geophysics, Chinese Academy of Sciences, Beijing, China, [2]School of Earth Sciences, Damghan University, Damghan, Iran, [3]CCFS and GEMOC ARC National Key Centre, Macquarie University, Sydney, NSW, Australia, [4]Now at GEOMAR, Helmholtz-Zentrum für Ozeanforschung Kiel, Kiel, Germany, [5]Geosciences Department University of Texas at Dallas, Richardson, TX, USA, [6]Centre for Geoscience, Universidad Nacional Autonoma de Mexico, Mexico City, Mexico, [7]Geobiotec. Departamento de Geociências, Universidade de Aveiro, Aveiro, Portugal, [8]Departamento de Geología, Centro de Investigación Científica y de Educación Superior de Ensenada (CICESE), Ensenada, Mexico, [9]University of Arizona, Tucson, AZ, USA, [10]Faculty of Geology and Geophysics, University of Bucharest, Bucharest, Romania

Abstract Most arcs show systematic temporal and spatial variations in magmatism with clear shifts in igneous rock compositions between those of the magmatic front (MF) and those in the backarc (BA). It is unclear if similar magmatic polarity is seen for extensional continental arcs. Herein, we use geochemical and isotopic characteristics coupled with zircon U-Pb geochronology to identify the different magmatic style of the Iran convergent margin, an extensional system that evolved over 100 Myr. Our new and compiled U-Pb ages indicate that major magmatic episodes for the NE Iran BA occurred at 110–80, 75–50, 50–35, 35–20, and 15–10 Ma. In contrast to NE Iran BA magmatic episodes, compiled data from MF display two main magmatic episodes at 95–75 and 55–5 Ma, indicating more continuous magmatism for the MF than for the BA. We show that Paleogene Iran serves as a useful example of a continental arc under extension. Our data also suggest that there is not a clear relationship between the subduction velocity of Neotethyan Ocean beneath Iran and magmatic activity in Iran. Our results imply that the isotopic compositions of Iran BA igneous rocks do not directly correspond to the changes in tectonic processes or geodynamics, but other parameters such as the composition of lithosphere and melt source(s) should be considered. In addition, changes in subduction zone dynamics and contractional versus extensional tectonic regimes influenced the composition of MF and BA magmatic rocks. These controls diminished the geochemical and isotopic variations between the magmatic front and backarc.

Plain Language Summary Most arcs show systematic temporal and spatial variations in magmatism with a clear shift in the composition of igneous products between those of the magmatic front and those in the backarc (BA). Our U-Pb ages for the NE Iran BA identify five magmatic episodes for the NE Iran backarc, which occurred at 110–80 million years ago (Ma), 75–50, 50–35, 35–20, and 15–10 Ma. The 110–80 Ma magmatic episode was a time of strong regional extension due to subduction initiation along the Zagros suture zone, while the younger episodes reflect maturation of the magmatic arc. The first magmatic episode is represented by magmas dominated by inputs from the underlying mantle, as does the next episode (75–50 Ma). The third pulse (50–35 Ma) shows increasing contributions from the underlying crust. The fourth magmatic pulse occurred at 35–20 Ma, and the volume of these magmas was less than other magmatic pulses. The final pulse in the NE Iran BA (15–10 Ma) suggests that there was a change in magmatic architecture beneath the BA. Magmatic pulses at 110–80 and 50–35 Ma accompanied extension, while others accompanied compression due to collision with Arabia. Contribution of continental crust components was highest for the 50–35 Ma magmatic episode.

1. Introduction

Arc magmatism at convergent margins is often episodic, involving steady low-volume magmatic lulls, which temporally changes into short-lived (5–20 Myr) high-volume flare-ups (Ducea et al., 2015b). Above subduction zones, volcanoes are concentrated along the magmatic front (MF) and also

distributed behind this, referred to as the "back-arc" and/or "rear-arc" magmatic realm. Some convergent margins have only a well-defined MF and little back-arc igneous activity. Others—like Iran in Late Cretaceous and Cenozoic time—have significant back-arc magmatism. Strong extension and attendant high-flux magmatism in MF and back-arc regions is expected to accompany spontaneous subduction initiation as a result of slab rollback (Stern, 2004; Stern & Gerya, 2018). Back-arc magmatism is a dominant process at some continental active margins, such as the Andes, Cascades, and eastern Eurasia (Churikova et al., 2001; Heydolph et al., 2012b; Jacques et al., 2013; Jacques et al., 2014). These arcs show systematic temporal and spatial variations in magmatism with a clear shift in igneous geochemistry between those of the MF and those in the backarc (BA). The across-arc variations include major elements, trace elements, and stable and radiogenic isotopes (e.g., Kuritani et al., 2008; Kuritani & Nakagawa, 2016). These across-arc geochemical variations may be caused by different processes including (a) variable degrees of partial melting beneath the MF and BA; (b) differences in mantle fertility due to convective flow within the mantle wedge from beneath the BA to the MF; and (c) differing proportions and compositions of fluids and melts liberated from the subducted slab (Kimura et al., 2010; Todd et al., 2011). Simultaneous magmatic activities in MF and BA are often related to subduction zones with strong extension in the overlying plate. Upper plate extension can be related to large-scale tectonic phenomena, such as change in plate convergence vectors, slab rollback, subduction initiation, subduction obliquity, slab break-off or change in slab dip.

The well-preserved Late Mesozoic-Cenozoic continental arc of Iran reveals spatial and temporal patterns of magmatism as well as across-arc geochemical variations in its magmatic evolution (Sepidbar et al., 2019). Iran is part of the Alpine-Zagros-Himalayan orogenic belt, which can be traced from the Alps, Carpathians, and Balkanides in the west through Turkey and the Caucasus eastward into Iran, the Lhasa terrane of Tibet, and into Indonesia. This orogen and magmatic arc formed in association with subduction of Neotethyan oceanic lithosphere below the southern Eurasian margin.

Igneous activity in Iran started in Late Cretaceous time and continues to the present. Magmatism was related to the subduction of the Neotethyan oceanic crust beneath Iran from Cretaceous to Oligocene and then due to the collision between Arabia and Iran beginning at ~25 Ma (McQuarrie & van Hinsbergen, 2013). There are several lines of evidence suggesting that Arabia-Iran collision began ~25 Ma ago, during the late Oligocene (Barber et al., 2018; Koshnaw et al., 2017; Koshnaw et al., 2019; McQuarrie & van Hinsbergen, 2013). The collision led to core complex exhumation and melting of Iranian crust (Moghadam, Rossetti, et al., 2016; Stockli, 2004). This is also about the time that Arabia rifted away from Africa and opened the Red Sea (Stern & Johnson, 2010). Apatite (U-Th)/He cooling ages of ~20 Ma from the Saghand region of central Iran suggest an early Miocene period of north–south shortening related to collision (Verdel et al., 2007). Subduction was accompanied by the development of a continental (Andean-type) magmatic arc, parallel, but ~150–200 km north of the Zagros suture zone (Main Zagros Thrust, Figure 1a), known as the Urumieh-Dokhtar Magmatic Belt (UDMB). The UDMB defines the MF associated with Neotethyan subduction. Magmatic rocks are also abundant to the NNE of the UDMB, which reflect BA magmatism. Available geochronological data indicate the UDMB experienced magmatic flare-ups in the Eocene (~54 Ma until 37 Ma, subduction-related magmatism) and in the Miocene (20–5 Ma, collision-related magmatism) (Chiu et al., 2013; Verdel et al., 2007). There are different explanations for the Eocene flare-up, including decompression melting of lithospheric mantle metasomatized by slab-derived fluids (Verdel et al., 2007) or break-off of the downgoing slab and delamination of thickened subcontinental lithospheric mantle (Pang et al., 2013). Similar to Iran, the Izu-Bonin-Mariana arc has also a well-defined MF and BA. Detailed studies have shown that there is a geochemical-isotopic asymmetry between the BA and the MF, where the BA shows more enriched compositions, more similar to the average continental crust (Ishizuka et al., 2003; Tamura et al., 2007). In contrast, the MF magmas are enriched in fluid-mobile, slab-derived components and depleted in mantle-derived fluid-immobile elements such as Nb-Ta (Tatsumi & Kogiso, 2003).

The Cenozoic UDMB is ideal for investigating the relationship of upper plate extension to magmatic flare-up and how these are manifested (or not) in the BA. We want to know whether magmatic flare-ups occurred at the same time in the MF and BA and what are the geochemical-isotopic differences between the MF and BA magmatic pulses. This study addresses the age, geochemical and isotopic signatures of these magmatic
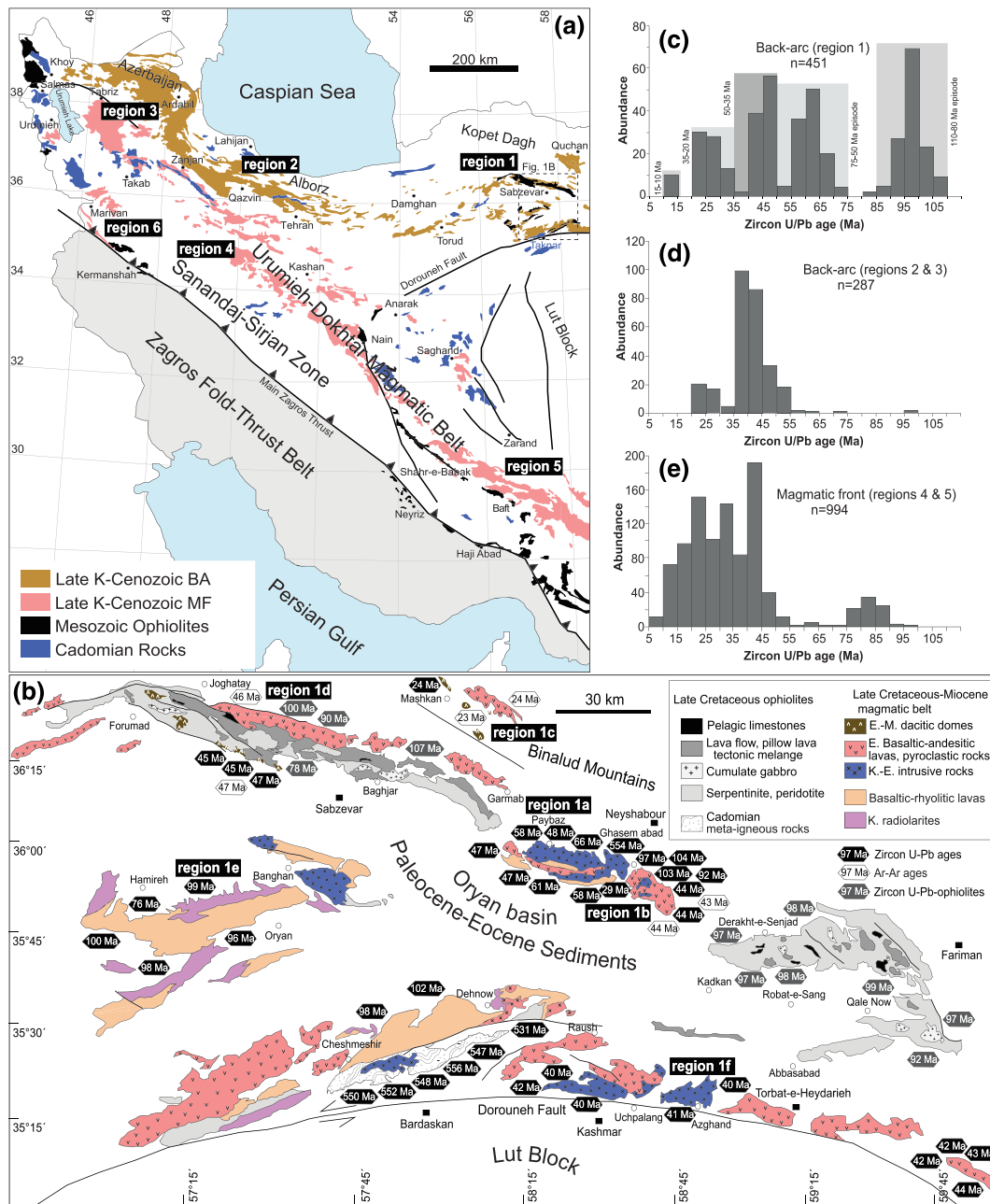
Figure 1. (a) Simplified geological map of Iran emphasizing Ediacaran-Early Cambrian (Cadomian) magmatic rocks, Mesozoic ophiolites, and Cenozoic magmatic rocks from back-arc and magmatic front. (b) Geological map of the Sabzevar-Torbat-e-Heydarieh region, north of the Dorouneh Fault, showing distribution of ophiolites and Mesozoic-Cenozoic back-arc rocks. Zircon U-Pb data on ophiolites are from Moghadam et al. (2014) and Moghadam et al. (2020). Zircon U-Pb data on the BA magmatic rocks from Region 1d are from Moghadam, Li, et al. (2016), Region 1f from Kazemi et al. (2019), and Region 1e from Moghadam, Li, et al. (2015). Cadomian rocks north of Bardaskan are from Moghadam, Li, Santos, et al. et al. (2017). Ar-Ar data of Region c are from Ahmadi et al. (2017). (c–e) Zircon U-Pb age histograms of the magmatic pulses from Iran magmatic fronts (Regions 4 and 5 in Figure 1a) and backarcs (Regions 1 to 3). Zircon U-Pb-Hf isotope results on Iran arcs are from (Aghazadeh et al., 2010; Aghazadeh et al., 2011; Castro et al., 2013; Chiu et al., 2013; Chiu et al., 2017; Moghadam, Li, et al., 2015; Moghadam, Li, et al., 2016; Moghadam, Griffin, et al., 2017; Sepidbar et al., 2018).

pulses. We present new zircon U-Pb ages as well as zircon O-Hf and bulk rock major-trace and Sr-Nd isotopic data for the NE Iran BA and compare these with compiled data from the MF (UDMB) and N-NW Iran BA. We use these insights to better understand magma genesis and element recycling associated with continental convergent margin magmatism.

2. Geological Setting

The continental crust of Iran mostly consists of Late Neoproterozoic-Early Cambrian rocks (e.g., Hassanzadeh et al., 2008; Moghadam, Li, Griffin, et al., 2017). These are related to Cadomian magmatism that occurred along the northeastern margin of Gondwanaland in an active continental margin. Cadomian igneous rocks also make up much of the crust of western Europe, where they are also referred to as Avalonian. Cadomian and Avalonian crust underlies large tracts of eastern N America and southern Europe (Linnemann et al., 2011). Cadomian crust can be traced eastwards into SE Europe, Turkey, and Iran and perhaps further into Central Asia (von Raumer et al., 2002). Cadomian magmatism in Iran began ~620 Ma and ended ~500 Ma, although most igneous activity occurred between 525 and 570 Ma (Moghadam, Khademi, et al., 2015; Moghadam, Griffin, et al., 2017; Moghadam, Li, Griffin, et al., 2017). Cadomian exposures are scattered across Iran (Figure 1a). That Iran is mainly underlain by Cadomian crust is supported by exposures of these rocks in core complexes (Ramezani & Tucker, 2003) and by basement uplifts (Moghadam et al., 2019). Inherited zircons as well as bulk rock Nd and zircon Hf model ages from Cenozoic magmatic rocks also confirm that Iran crust mainly consists of Cadomian magmatic rocks (e.g., Moghadam et al., 2018; Sepidbar et al., 2018; Sepidbar et al., 2019). Cadomian crust is important as assimilant for the evolution of Cenozoic magmas. However, we do not rule out that the crust beneath Iran is heterogenous and there may be some older continental ribbons such as NE (Alizadeh et al., 2017), SE (Moghadam, Brocker, et al., 2017), and central Iran (Shakerardakani et al., 2019). Pre-Cadomian crust, if it exists, has yet to be discovered.

Cadomian-Avalonian fragments rifted from northern Gondwana during the Paleozoic and later accreted to Laurasia (Murphy et al., 2004; Nance et al., 2010; Neubauer, 2002; Pereira et al., 2006; Skipton et al., 2013; von Raumer et al., 2003; Zulauf et al., 1997). Iran and Anatolia separated from northern Gondwana during the Permian and collided with Eurasia during the Cimmeride orogeny (Late Triassic) (Stampfli et al., 1991; Zanchi et al., 2015).

Late Cretaceous-Cenozoic igneous rocks are widespread in Iran and occupy a region that is up to 1,000 km broad from west to east (Azerbaijan-Alborz) and from north (south of Kopet Dagh; the BA) to south (UDMB; the MF) (Figure 1a). Magmatic arcs are commonly this long but rarely this wide. All of these magmatic rocks formed in response to northward subduction of Neotethys oceanic lithosphere; delamination of the overriding plate and/or break-off of the subducting slab may also have contributed to magmatism. Jurassic-Early Cretaceous magmatic rocks also occur in the Sanandaj-Sirjan Zone (SaSZ). The SaSZ extends as a NW-SE trending belt (~1,500 km long and ~150–200 km wide) across southern Iran and consists of Phanerozoic magmatic, metamorphic, and sedimentary rocks (Figure 1a). The SaSZ was interpreted to represent a Jurassic magmatic arc, but it is increasingly recognized as a continental rift (e.g., Azizi et al., 2018; Azizi & Stern, 2019; Burg, 2018; Hunziker et al., 2015; Lechmann et al., 2018).

Geochronological and geochemical data from Zagros ophiolites strongly support Neotethyan subduction initiation during Late Cretaceous and maturation in Latest Cretaceous and Cenozoic (e.g., Golonka, 2004; Moghadam & Stern, 2011, 2015; Monsef et al., 2018; Nouri et al., 2016). Subduction initiation in Zagros was coincident with equivalents in Oman and the Mediterranean area (Cyprus, Turkey, Syria to Iraq) (Moghadam & Stern, 2011; van Hinsbergen et al., 2019). The above summary may be controversial, but there is little doubt that Latest Cretaceous and Cenozoic magmatic rocks are related to subduction of Neotethys beneath Iran. Below we subdivide the Latest Cretaceous-Cenozoic Iran arc into MF, BA, and NE Iran BA and discuss these three subprovinces separately.

2.1. MF

The UDMB is a 50–80 km wide volcano-plutonic belt that defines the MF and trends NW-SE for >1,000 km across Iran between 28°N and 39°N (Figure 1a). The UDMB evolved for ~100 Ma, from when subduction began in Late Cretaceous time, continuing as a mature arc in Paleogene with a magmatic flare-up during the Eocene (Moghadam, Griffin, et al., 2017), before changing magmatic style again following the beginning of collision with Arabia during Late Oligocene-Miocene. The UDMB comprises thick (~4 km) sequences of calc-alkaline, shoshonitic, and adakitic lavas and pyroclastic rocks. Calc-alkaline and shoshonitic igneous rocks are widespread in the UDMB. These igneous rocks formed as compositionally distinct pulses. The UDMB arc began in Late Cretaceous time with eruption of low-K tholeiitic and calc-alkaline magmas.

Late Cretaceous calc-alkaline granitoids are also reported from SE UDMB (Hosseini et al., 2017). Early Paleocene time was a magmatic lull accompanying uplift of Zagros forearc ophiolites. Middle to Late Paleocene igneous rocks have calc-alkaline characteristics but analyses are sparse because eruptions were explosive, depositing thick pyroclastic rocks. Abundant Eocene igneous rocks are dominantly high-K calc-alkaline. Magmas became shoshonitic during Oligocene-Middle Miocene time. Late Miocene to Plio-Quaternary UDMB igneous rocks have adakitic and ultrapotassic geochemical signatures (Pang et al., 2015; Pang et al., 2016). Eocene plutonic rocks are barren, while Miocene intrusions contain Cu-Au mineralization. Eocene lavas can be subaerial, intercalated with pyroclastic rocks or shallow submarine, interlayered with Eocene *Nummulites*-bearing limestones and tuffs (Verdel et al., 2011a). Late Cretaceous magmatic rocks are also reported from the NW segment of the SaSZ (east of Marivan and south Urumieh, Figure 1a) (Azizi & Jahangiri, 2008; Ghalamghash et al., 2009), whereas Eocene volcanic rocks are present also along the Main Zagros Thrust (e.g., Ali et al., 2013). Both are related to the subduction of Neotethys beneath the Iranian plateau and formed in a MF context.

2.2. Back-Arc Magmatic Belt

Back-arc igneous activity occurred along a NW-NE arcuate belt (>1,200 km long, Figure 1a) during the Late Cretaceous to Eocene, with eruption of marine to subaerial magmatic rocks (Ballato et al., 2011; Verdel et al., 2011b). Different plutonic pulses are also recorded in BA regions. There are different geodynamic interpretations for the formation of magmatic rocks in Iran BA. The first hypothesis considers that igneous rocks of the Iran MF (UDMB) and BA are related to a single Neotethyan subduction zone (e.g., Moghadam et al., 2018; Sepidbar et al., 2019; Verdel et al., 2011b), whereas a second interpretation calls for two or more subduction zones, one or more related to the subduction of back-arc oceanic lithosphere beneath NE and NW Iran (e.g., Ghasemi & Talbot, 2006). However, seismic and mantle tomography data are most consistent with a single, N-dipping subduction zone (e.g., Al-Lazki et al., 2004; Authemayou et al., 2006; Entezar-Saadat et al., 2017; Molinaro et al., 2005; Shomali et al., 2011). Another subduction zone may have existed beneath eastern Iran to close a small oceanic basin associated with the Birjand-Zahedan ophiolite belt, and some Late Cretaceous arc igneous rocks in eastern Iran may be related to this (e.g., Pang et al., 2012; Pang et al., 2013). Description of the Paleogene magmatic rocks of eastern Iran and their genesis triggers are beyond this study.

Paleogene back-arc extension and magmatism developed in response to subduction along the Zagros trench. This extension is also reflected by several transgression-regression cycles recorded in latest Cretaceous to Eocene BA sediments (Figure 2d) (Ballato et al., 2011). Middle to Late Paleocene time witnessed marine regression followed by deposition of red (terrestrial) volcano-sedimentary sequences. Early to middle Eocene witnessed marine transgression in NE Iran, with deposition of thick (500–1,000 m) sequences of deep marine *Nummulites*-bearing limestones (Moghadam, Li, et al., 2015). The thickness of these limestones varies in different parts of Iran and grade upwards into fine-grained pyroclastic rocks.

Late Cretaceous-Neogene arc magmatism across the Iran arc—both MF and BA—was compositionally heterogeneous (e.g., Sepidbar et al., 2019). Igneous rocks of intermediate to acidic (often pyroclastic) composition dominate the MF, although mafic rocks are also found (Figure 2a). In contrast, basaltic rocks are more abundant in the NW BA than are felsic rocks (Figure 2b), whereas felsic rocks dominate in the NE BA (Figure 2c). High-K rocks and shoshonites occupy a vast region in the Iran BA (Asiabanha & Foden, 2012; Castro et al., 2013; Ghorbani et al., 2014; Moghadam et al., 2018).

2.3. Back-Arc Magmatism in NE Iran

Magmatism in the NE Iran BA started in the latest Cretaceous and continued into Paleogene-Neogene time, but there has not yet been a systematic geochronological study of these rocks. They are distributed north and south of the Sabzevar-Torbat-e-Heydarieh ophiolitic belt (STHOB) and also intrude the ophiolites to the north and south (Figure 1b). The STHOB is considered as a Late Cretaceous back-arc oceanic basin associated with subduction initiation along what is now the Zagros orogen (Moghadam et al., 2020).

Late Cretaceous igneous rocks are abundant in NE Iran BA (Figure 1b). These are largely marine, comprising rhyolitic to dacitic (with rare andesitic) lavas, felsic tuffs, and radiolarites. Subaerial lavas including alternating basalts and dacites are also common. These are overlain by both Middle Paleocene-Eocene terrigenous sediments (Oryan basin; Figure 1b) and Mid-Late Paleocene-Eocene acidic to intermediate
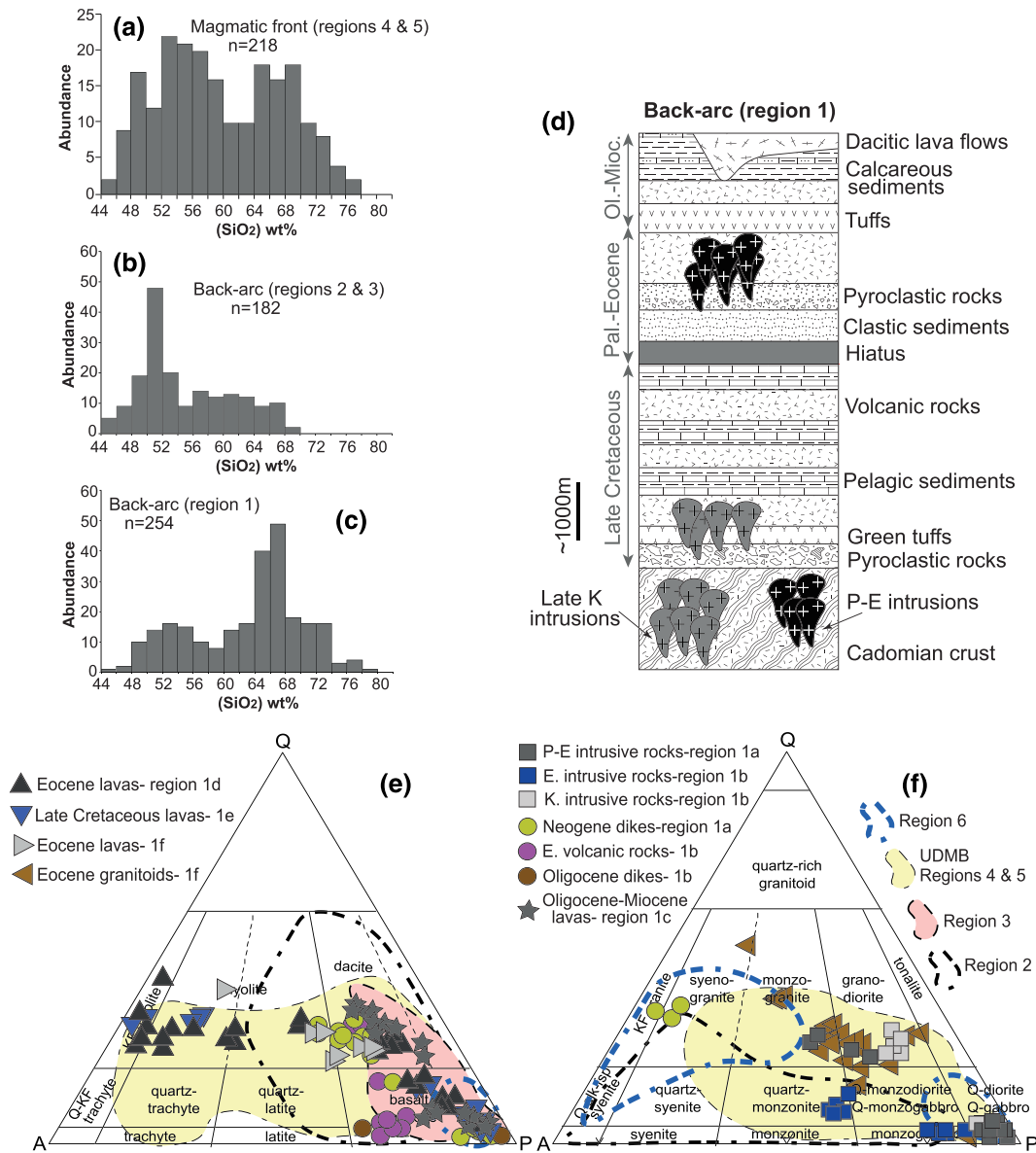
Figure 2. (a–c) Compositional variations of igneous rocks from the Iran magmatic front and backarc. Data for Regions 2 and 3 are from Aghazadeh et al. (2010), Aghazadeh et al. (2011), Asiabanha et al. (2009), Asiabanha and Foden (2012), Castro et al. (2013), and Moghadam, Griffin, et al. (2017). Data on Regions 4 and 5 are from Alavijeh et al. (2017), Honarmand et al. (2013), Moghadam, Li, et al. (2015), Moghadam, Li, et al. (2016), and Sepidbar et al. (2018). (d) Lithological section showing the relationships between rock units from the NE Iran BA. (e, f) Quartz-alkali feldspar-plagioclase (QAP) (Streckeisen, 1979b) diagram for classifying NE Iran volcanic (e) and plutonic (f) rocks.

pyroclastic rocks with intercalated mafic to andesitic lavas (Figure 2d). In the NE BA, Late Cretaceous-Paleogene intrusions were emplaced into thick sequences of Cretaceous terrigenous sediments as well as pyroclastic and volcanic rocks. These plutons also intrude Late Neoproterozoic igneous rocks (Figure 2d).

There are some radiometric ages for NE Iran BA magmatic rocks, but the ages of many magmatic bodies remain unclear. To better resolve the timing of NE Iran BA magmatism, new zircon U-Pb ages were obtained by secondary ion mass spectrometry and laser ablation-inductively coupled plasma-mass spectrometry from 22 representative magmatic rocks. Two $^{40}Ar/^{39}Ar$ ages were also obtained from mineralized Paleogene igneous rocks. In situ hafnium and oxygen isotope data were obtained on selected zircon grains. Representative rocks were also analyzed for major and trace element compositions and Sr-Nd isotopes.

The complete analytical details are provided in Text S2 in the supporting information. These results are compared with ages and geochemistry of MF rocks and used to discuss the Late Cretaceous and Cenozoic magmatic evolution of the NE Iran BA.

3. Geological and Geochronological Characteristics of NE Iran Back-Arc Magmatism

To better characterize the age and composition of these rocks, we selected six regions for study (Regions 1a to 1f; Figure 1b). Each of the six studied areas tells a different story. Two study areas are dominated by Late Cretaceous igneous rocks, three are dominated by Paleocene-Eocene igneous rocks, and one is dominated by Oligocene-Miocene igneous rocks (Figures 1c–1e). A summary of geological and geochronological characteristics is presented below and summarized in Table 1.

Region 1a (Paybaz complex, PC) includes deep-seated intrusions of mafic to felsic rocks, dikes, volcanic rocks as well as hornblende-rich (appinitic) segregations and layers (4–5 to ~>30 cm thick). Appinitic segregations and layers occur within the granitoids. In the modal quartz-alkali feldspar-plagioclase diagram (Streckeisen, 1979a), PC intrusive rocks have gabbro-diorite to granodiorite-granite compositions (Figure 2f). PC dikes are compositionally variable and plot predominantly in the field of basalt-andesite to dacite-rhyolite (Figure 2e). Aplitic dikes show granitic composition (Figure 2f). Possibly, coeval volcanic rocks of Paleogene age are also present south of the PC. Volcanic rocks range in composition from basalt to porphyritic andesites (Figure S1f). Detailed petrography is presented in Text S1. Zircon U-Pb ages for Paybaz complex granitoids and dikes show multiple ages. Fine-grained PC granites show $^{206}Pb/^{238}U$ weighted mean age of 62.4 $\pm$ 0.6 Ma, while PC granodiorites have $^{206}Pb/^{238}U$ age of 65.8 $\pm$ 0.9 Ma (Figure 3). Hornblendite (appinite) layers in PC granitoids have $^{206}Pb/^{238}U$ ages of 58.5 $\pm$ 0.9 and 57.6 $\pm$ 0.7 Ma. Deformed as well as coarse-grained gabbros have $^{206}Pb/^{238}U$ ages of 48 $\pm$ 0.6 and 47 $\pm$ 0.5 Ma, respectively (Figures 3 and 4). Dacitic dikes within the PC intrusion have older zircons with weighted mean $^{206}Pb/^{238}U$ age of 47 $\pm$ 0.6 Ma, whereas younger zircons yield 11.9 $\pm$ 0.2 Ma. Younger ages show the crystallization age of this dike, whereas the older zircons (47 Ma) are inherited. Diabasic-andesitic dikes also contain younger zircons with ages of 12.7 to 14.9 Ma, but zircons as old as 788 Ma are also present.

Region 1b (Ghasem Abad complex, GC) contains Late Cretaceous coarse-grained green amphibole-bearing diorite (Figure S2d) to Eocene granodiorite and porphyritic monzogabbro-monzodiorite to quartz monzonite. Late Cretaceous amphibole-bearing granitoids plot in both diorite and granodiorite fields in the QAP diagram (Figure 2f), whereas younger shallow intrusions show monzogabbro-monzodiorite to quartz monzonite compositions (Figure 2f). Eocene volcanic rocks are also present in GC and mostly have andesitic compositions in the QAP diagram, whereas dacites are rare (Figure 2e). The occurrence mode of volcanic and plutonic rocks is summarized in Table 1, whereas detailed sample petrography is presented in Text S1. Oligocene intermediate to mafic dikes crosscut the porphyritic andesites and shallow intrusive rocks (Figure S2e). Coarse-grained amphibole-bearing diorites are the oldest GC igneous rocks, with zircon $^{206}Pb/^{238}U$ ages of 104 $\pm$ 1.4 to 102.8 $\pm$ 1.2 Ma as well as 96.9 $\pm$ 0.8 and 92.1 $\pm$ 1.2 Ma. GC porphyritic monzogabbro yields a $^{206}Pb/^{238}U$ age of 44.2 $\pm$ 0.4 Ma, while hydrothermally silicified granitoids are 44–48 Ma. Andesitic lavas yield a weighted mean $^{206}Pb/^{238}U$ age of 44.1 $\pm$ 0.4 Ma, although slightly older zircon antecrysts (~45 Ma) are also present. Amphibole from trachyandesite yield ^{40}Ar-^{39}Ar age of 42.70 $\pm$ 0.19 Ma (Figure S6), which is significantly younger than the zircon U-Pb result obtained from this sample (44.1 $\pm$ 0.4 Ma). We also dated hydrothermal biotites using ^{40}Ar-^{39}Ar method from narrow potassic zones around the monzo-gabbroic to monzo-dioritic porphyry stocks (with U-Pb age of 44.2 $\pm$ 0.4 Ma). Laser step-heating experiments on biotite concentrates yield an age of 43.68 $\pm$ 0.14 Ma (Figure S6), which is only slightly younger than the zircon U-Pb ages for the porphyry stocks. Intermediate to mafic dikes with weighted mean age of 29.4 $\pm$ 0.2 Ma are the youngest GC magmatic pulses.

Region 1c (Mashkan complex, MC) includes Oligocene-Miocene mafic-intermediate lavas as well as felsic domes. In the QAP diagram, MC igneous rocks show dacitic-andesitic to basaltic compositions (Figure 2e). Geochemically, these rocks are classified as high-Mg basaltic andesites to dacites as well as high-Nb hawaiites and mugearites (Ahmadi et al., 2017). Whole rock $^{40}Ar/^{39}Ar$ ages of 24.1 $\pm$ 0.4 and 22.9 $\pm$ 0.5 Ma are reported for the volcanic rocks (Ahmadi et al., 2017). We dated one MC dacitic lava flow using secondary ion mass spectrometry. Zircons from this sample yielded a weighted mean $^{206}Pb/^{238}U$ age of

Table 1
Summary of Geological Characteristics and Zircon U-Pb Ages of Back-Arc Magmatism From NE Iran

Geological area	Geological characteristics	Zircon $^{206}Pb/^{238}U$ weighted mean age
Region 1a Paybaz complex (PC)	Mafic to felsic intrusions with abundant dikes and volcanic rocks. Intrusions are characterized by foliated diorites and gabbros along the margin and coarse-grained diorites to granites in the centers (Figure S1a and S1b). Abundant hornblende-rich (appinitic) segregations and layers (4–5 to ~>30 cm thick) within the granitoids at the center of intrusions (Figures S2a and S2b). Different types of dikes are also common, including aplite (Figure S1c) diabase, andesite, and dacite (Figures S1d and S1e). Volcanic rocks of Paleogene ages are also present south of the PC.	Fine-grained granites show age of 62.4 ± 0.6 Ma. Granodiorites have age of 65.8 ±0.9 Ma. Hornblendite (appinite) layers show ages of 58.5 ± 0.9 and 57.6 ± 0.7 Ma. Deformed and coarse-grained gabbros have ages of 48 ± 0.6a and 47 ± 0.5 Ma. Dikes show ages of 11.9 to 14.9 Ma.
Region 1b Ghasem Abad complex (GC)	Contain both intrusive and volcanic rocks (Figure S2c). Intrusive rocks vary from coarse-grained green amphibole-bearing diorite (Figure S2d) to granodiorite and porphyritic monzogabbro-monzodiorite to quartz monzonite. Leuco-granitic dikes intrude the coarse-grained green amphibole-bearing diorites-granodiorites. Shallow monzogabbro-monzodiorite to quartz monzonitic stocks occurs within both volcanic and pyroclastic rocks and also within the coarse-grained Late Cretaceous diorite-granodiorite. There is evidence of Cu mineralization associated with monzogabbro-monzodiorite to quartz monzonitic pulses. Porphyritic andesitic to basaltic volcanic rocks are abundant and contain plagioclase and hornblende porphyries. Dacitic lavas with sanidine phenocrysts are rare. Minor pyroclastic rocks is found in the eastern parts of GC. Oligocene intermediate to mafic dikes crosscut the porphyritic andesites and shallow intrusive rocks (Figure S2e). Most volcanic and shallow intrusive rocks suffered argillic and propylitic alteration (Figure S2f), especially south of the GC. Silicification is also common. Shallow monzogabbro-monzodiorite to quartz monzonitic intrusions show minor potassic alteration in some places, with abundant fine-grained biotite. Gold-bearing, quartz-adularia-calcite veins are present south of the GC and may be associated with Oligocene dikes.	Coarse-grained amphibole-bearing diorites have ages of 104 ± 1.4, 102.8 ± 1.2, 96.9 ± 0.8, and 92.1 ± 1.2 Ma. Porphyritic monzogabbros yields age of 44.2 ± 0.4 Ma, while silicified granitoids are 44–48 Ma. Andesitic lavas have age of 44.1 ±0.4 Ma. Intermediate dikes show age of 29.4 ± 0.2 Ma.
Region 1c Mashkan complex (MC)	Oligocene-Miocene mafic lavas are in close association with felsic lava flows as well as domes. Felsic domes were injected both into the mafic-intermediate volcanic rocks and into the Miocene detritus and calcareous sediments (Figure S3a). Minor pyroclastic rocks are highly altered. Most dacitic domes are aphyric, although some contain sanidine phenocrysts. Mafic and	Dacitic lavas have zircon U-Pb age of 24.2 ± 0.3 Ma.

Table 1
(continued)

Geological area	Geological characteristics	Zircon ^{206}Pb/^{238}U weighted mean age
	intermediate rocks are also aphyric to olivine-clinopyroxene phyric.	
Region 1d Joghatay complex (JC)	This area consists of Eocene volcanic, hypabyssal, and plutonic rocks and are distributed north and south of the Sabzevar ophiolite (Figure 1b). JC volcanic rocks are mafic to acidic. Dacitic to rhyolitic hypabyssal domes intrude older pyroclastic rocks as well as the Sabzevar ophiolites and are unconformably overlain by Neogene to Quaternary immature sedimentary rocks. Volcanic rocks are aphyric to porphyritic. Plutonic rocks are rare and mostly granitic. Lapilli tuffs, agglomerates, and volcanic breccias are also common.	Dacitic to rhyolitic domes show ages of 45.5 ± 0.9, 46.8 ± 0.7, and 45.3 ± 0.7 Ma.
Region 1e Oryan complex (OC)	This area comprises Late Cretaceous intermediate (andesite) to felsic (dacite-rhyolite) submarine lavas with intercalated radiolarites, cherts, siliceous shales, and green tuffs. Late Cretaceous pelagic sediments also cover lavas. This area also contains alternating Late Cretaceous basaltic to dacitic lavas and terrigenous sediments that conformably overlie coarse-grained pyroclastic rocks and green tuffs (Figures 2d and S3b). Variably altered granitic-dioritic and minor gabbroic bodies intrude Late Cretaceous pyroclastic rocks and rare lavas (Figure S3c and S3d). Volcanic rocks grade downward into mixed pyroclastic rocks and pelagic sediments.	Granites have ages of 96.2 ± 0.4, 98.03 ± 0.68, 101.9 ± 1, and 100.44 ± 0.95 Ma. Diorites show age of 75.78 ± 0.29 Ma, while rhyolites and dacites have age of 99.2 ± 2.5 and 98.0 ± 0.4 Ma.
Region 1f Kashmar complex (KC)	Includes Eocene shallow leucogranites-granodiorites to monzogranites. These intrusions contain centimetric (~10–20 cm) to metric (~1 m) aplitic and microgranodioritic dikes (Figure S3f). The granitoids intrude Paleocene-Eocene pyroclastic and early to middle Eocene mafic to felsic volcanic rocks that erupted subaerially. All these rocks seem to have been injected into Late Neoproterozoic-Early Cambrian (Cadomian, 531–556 Ma) igneous and metasedimentary rocks.	Intrusive rocks show ages of 41.9 ± 0.3, 39.9 ± 0.5, and 40.5 ± 0.6 Ma. Aplitic dikes yield age of 40.1 ± 0.5 and enclaves has age of 40.5 ± 0.4 Ma. Volcanic rocks show ages of 42.4 ± 0.6, 42.7 ± 0.5, 43.5 ± 0.6, 43.6 ± 0.9, and 42.6 ± 0.5 Ma.

24.2 ± 0.3 Ma. This agrees with the bulk rock ^{40}Ar-^{39}Ar ages of 24.1 ± 0.4 and 22.9 ± 0.5 Ma for the intermediate to felsic volcanic rocks (Ahmadi et al., 2017).

Region 1d (Joghatay complex, JC) igneous rocks consist of Eocene volcanic, hypabyssal, and plutonic rocks. In the QAP diagram, JC volcanic rocks show rhyolitic-dacitic to basaltic compositions (Figure 2e). Available zircon U-Pb and amphibole-biotite ^{40}Ar-^{39}Ar ages from the JC show a single middle Eocene magmatic pulse. JC acidic domes show ^{206}Pb/^{238}U ages of 45.5 ± 0.9, 46.8 ± 0.7, and 45.3 ± 0.7 Ma. White mica from the rhyolitic domes yield a ^{40}Ar-^{39}Ar age of 46.75 ± 0.26 Ma, while biotite from intermediate lava flows shows a ^{40}Ar-^{39}Ar age of 46.44 ± 0.11 Ma (Moghadam, Li, et al., 2016).
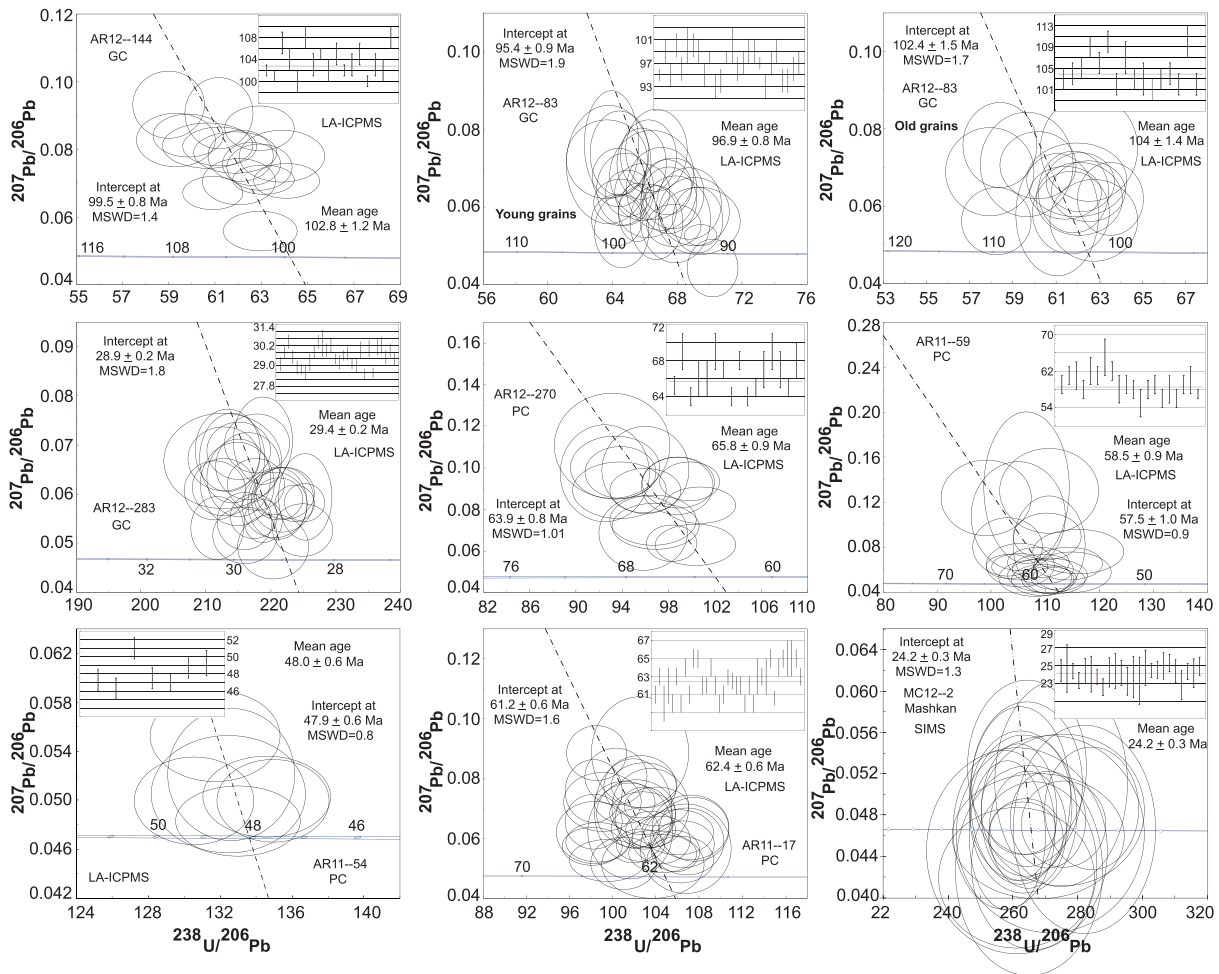
Figure 3. U-Pb inverse-concordia (^{207}Pb/^{206}Pb vs. ^{238}U/^{206}Pb) and weighted mean ^{206}Pb/^{238}U ages for zircons from NE Iran BA magmatic rocks.

Region 1e (Oryan complex, OC) contain Late Cretaceous intermediate to felsic submarine lavas with intercalated radiolarites, cherts, siliceous shales, and green tuffs. Late Cretaceous basaltic to dacitic lavas and interlayered terrigenous sediments are also present. Granitic-dioritic and minor gabbroic bodies also occur in OC. These rocks show fault contacts with Late Cretaceous STHOB peridotites and are underlain by Cadomian continental crust. In the QAP diagram, the OC Late Cretaceous igneous rocks are bimodal and display rhyolitic-dacitic as well as andesitic-basaltic compositions (Figure 2e). Available data from OC granites indicate ^{206}Pb/^{238}U ages of 98.03 ± 0.68, 101.9 ± 1, and 100.44 ± 0.95 Ma. OC diorites show a ^{206}Pb/^{238}U age of 75.78 ± 0.29 Ma, while rhyolites have zircons with ^{206}Pb/^{238}U age of 99.2 ± 2.5 Ma (Kazemi et al., 2019). New zircon U-Pb data confirm these ages. Granitic intrusion and dacitic lavas in the OC have zircon ^{206}Pb/^{238}U ages of 96.2 ± 0.4 and 98.0 ± 0.4 Ma, respectively (Figure 1b and Text S1).

Region 1f (Kashmar complex, KC) includes Eocene leucogranites-granodiorites to monzogranites. The granitoids intrude Paleocene-Eocene pyroclastic and early to middle Eocene mafic to felsic volcanic rocks. In the QAP diagram, Eocene lavas are rhyolitic to dacitic (Figure 2e), while plutonic rocks have leucogranitic-granitic to tonalitic as well as monzodioritic compositions (Figure 2f). Zircon U-Pb data for KC monzogranites and granodiorites show ^{206}Pb/^{238}U ages of 41.9 ± 0.3, 39.9 ± 0.5, and 40.5 ± 0.6 Ma. Aplitic dikes yield a ^{206}Pb/^{238}U age of 40.1 ± 0.5 Ma, while a granodioritic enclave has an age of 40.5 ± 0.4 Ma (Moghadam, Li, et al., 2015). Volcanic rocks from the eastern KC show zircon ^{206}Pb/^{238}U ages of 42.4 ± 0.6, 42.7 ± 0.5, 43.5 ± 0.6, 43.6 ± 0.9, and 42.6 ± 0.5 Ma. These agree with published ^{206}Pb/^{238}U ages of 41.5 ± 0.6 Ma for intrusive rocks from this region (Sepidbar et al., 2018).
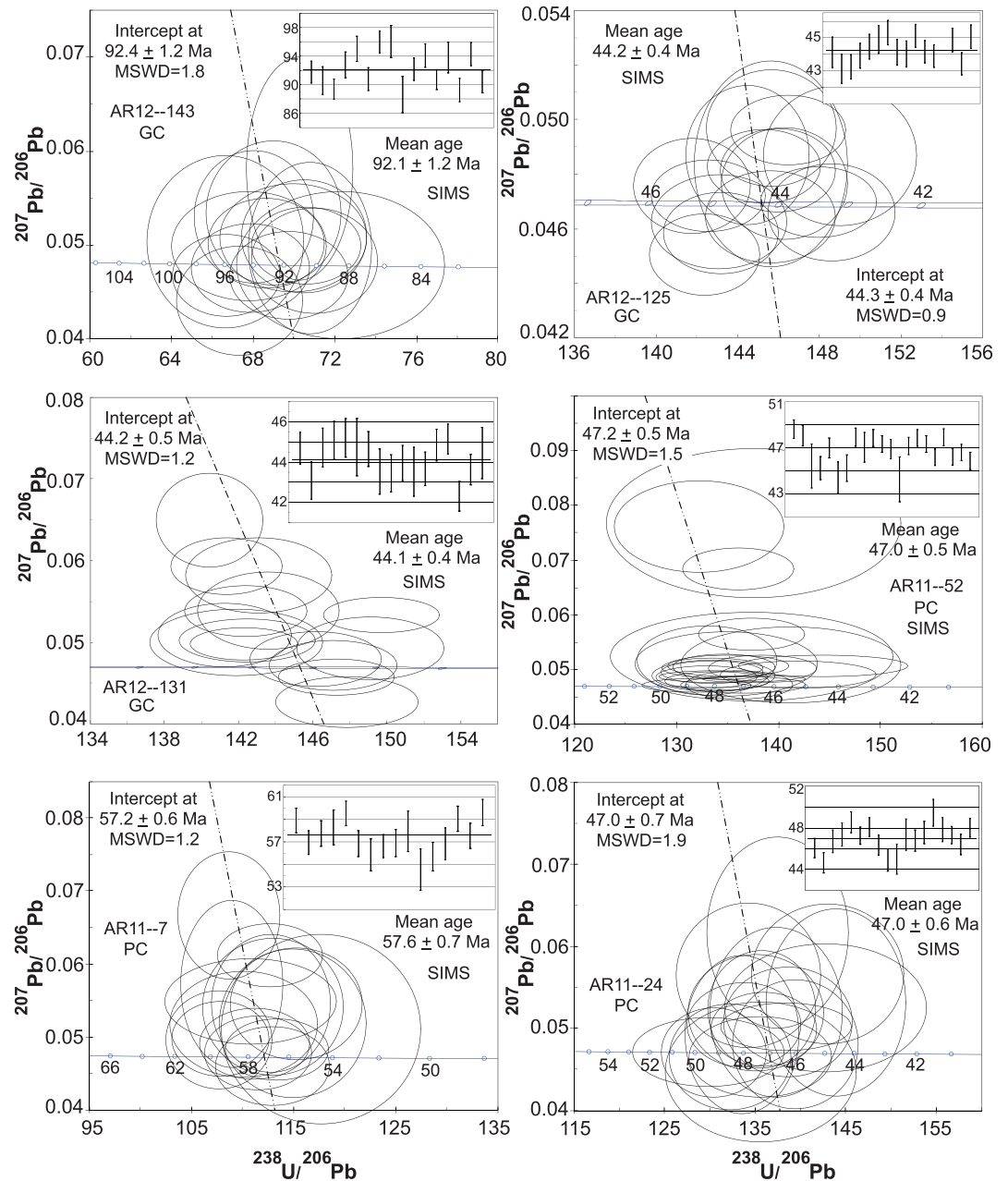
Figure 4. U-Pb inverse-concordia ($^{207}Pb/^{206}Pb$ vs. $^{238}U/^{206}Pb$) and weighted mean $^{206}Pb/^{238}U$ ages for zircons from NE Iran BA magmatic rocks.

4. Geochemical Characteristics of Magmatic Episodes From NE Iran BA

Our new zircon U-Pb ages help reveal five magmatic episodes in the NE Iran BA: 110–80, 75–50, 50–35, 35–20, and 15–10 Ma (Figure 1c). Below we describe the geochemical characteristics of each episode.

4.1. The 110–80 Ma Magmatic Episode

This episode comprises GC intrusive rocks and OC volcanic rocks. GC rocks have 56.2–68.4 SiO_2 wt.% and low (1.5–2.7 wt. %) K_2O. They have dioritic to granodioritic compositions in the $K_2O + Na_2O$ versus SiO_2 diagram (Figure 5a) and are calc-alkaline in the K_2O versus SiO_2 diagram (Figure 5c). These rocks have high Th/Yb ratios, similar to other arc igneous rocks (Figure 6a). Their Sr/Y ratio is low (12.1–35.4) and
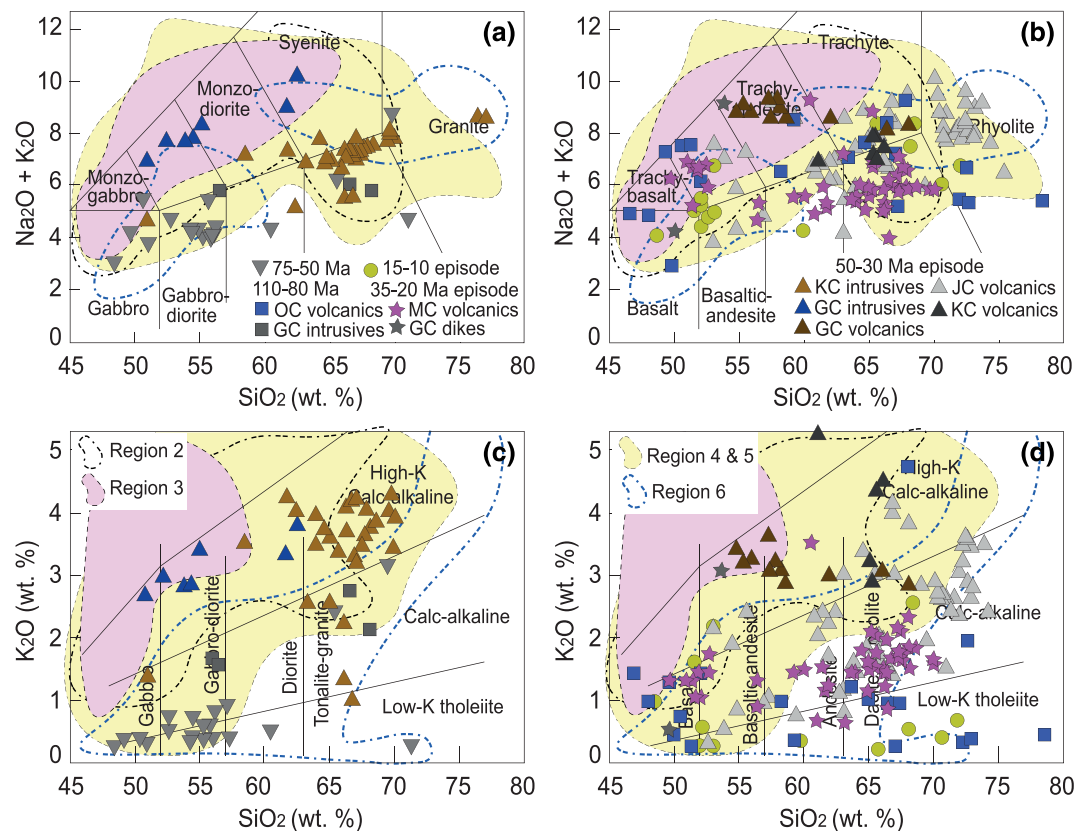
Figure 5. $Na_2O + K_2O$ and K_2O versus SiO_2 discrimination diagrams for the classification of plutonic (a, c) and volcanic (b, d) rocks from NE Iran back-arc rocks (modified after Lebas et al., 1986). Igneous rocks from different magmatic episodes are presented by distinctive symbols.

nonadakitic (Figure 6c). Compared to N-MORB, these granitoids are enriched in LREE relative to HREE ($La_{(n)}/Yb_{(n)} \sim 2.1$–3.6) (Figure 7a) and in Rb, Ba, Th, and U and are depleted in Nb-Ta (Figure 7b).

Late Cretaceous volcanic rocks show variable compositions in the $K_2O + Na_2O$ versus SiO_2 diagram (Figure 5b), ranging from basalt to trachy-basaltic andesite to trachy-andesite as well as dacite-rhyolite and trachyte and have low-K tholeiitic to high-K calc-alkaline signatures (Figure 5d). These rocks show both MORB-like (low Th/Yb ratio, ~0.1–0.8) and arc-like (high Th/Yb ratio, ~1.7–4.3) compositions (Figure 6b). Their Sr/Y ratios are low (~1.3–47.9) and nonadakitic (Figure 6d), except two samples with high Sr/Y ratios of 117 and 243. Compared to N-MORB, these volcanic rocks have depleted to enriched REE patterns (e.g., $La_{(n)}/Yb_{(n)} = 0.3$–12.3) (Figure 7e), are depleted in Nb-Ta (e.g., $Nb_{(n)}/La_{(n)} = 0.2$–0.7), and enriched in Th, Cs, and Ba (Figure 7f), except one sample with high Nb-Ta content ($Nb_{(n)}/La_{(n)} = 1.8$).

4.2. The 75–50 Ma Magmatic Episode

The latest Cretaceous-Paleocene magmatic episode includes PC intrusive rocks. These have variable SiO_2 (48.1–70.4 wt.%), Al_2O_3 (~14–20 wt. %), K_2O (0.2–3.1 wt. %), and Mg# (13.1–40.5). They are gabbroic to granitic on the $K_2O + Na_2O$ versus SiO_2 diagram (Le Maitre et al., 2002) (Figure 5a). Most have low K_2O content and plot within the low-K tholeiitic domain in the K_2O versus SiO_2 diagram, except two granitic samples with more K_2O (2.3–3.1 wt.%, Figure 5c). Th/Yb ratio for these intrusive rocks varies from 0.2 to 2.8. In the Th/Yb versus Nb/Yb diagram, these rocks show similarities both to the subduction-modified rocks and non-subduction-related rocks (Figure 6a). They have variable Sr contents (128–696 ppm) and Sr/Y ratio (4.9–43.8), similar to normal arc igneous rocks (Figure 6c). They are variably enriched in LREE, with $La_{(n)}/Yb_{(n)} \sim 0.7$–5.6 (Figure 7a). Most rocks are characterized by slight depletion or enrichment in Eu. These rocks have positive anomalies in Th, U, and negative anomalies in Nb and Ta relative to N-MORB (Figure 7b).
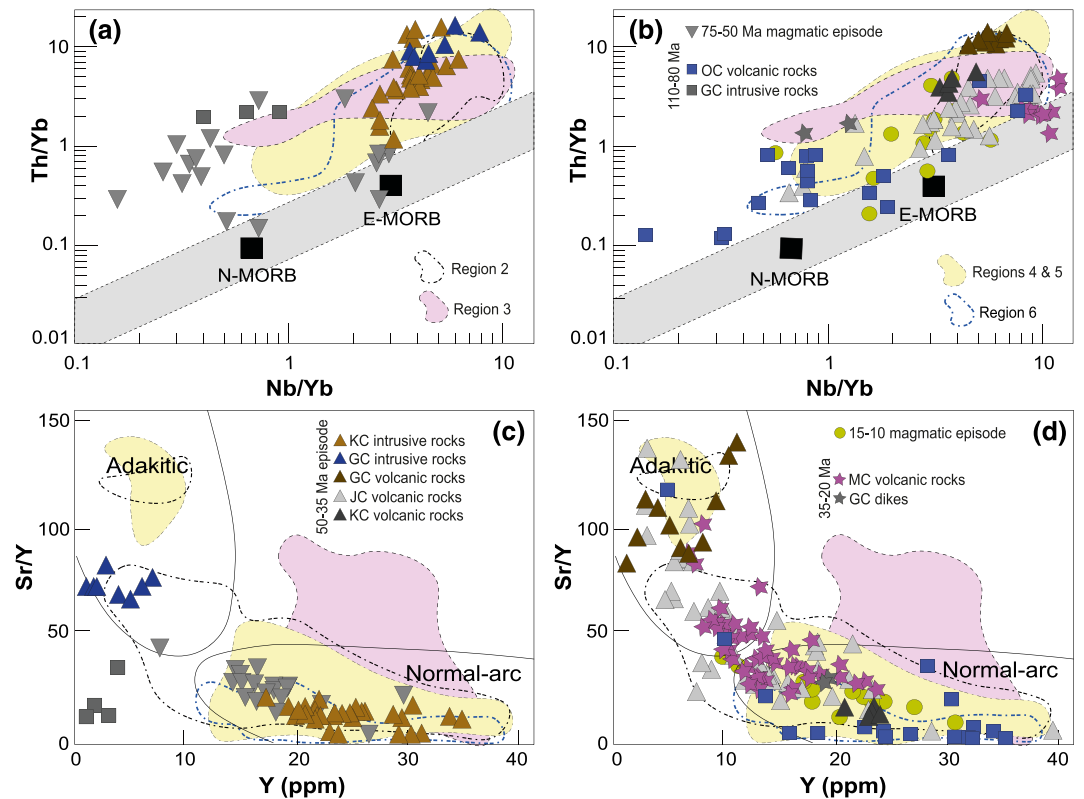
Figure 6. Th/Yb versus Nb/Yb and Sr/Y versus Y diagrams for discriminating plutonic (a, c) and volcanic (d, d) rocks from NE Iran backarc (the compositional domains for adakite and normal island-arc dacites and rhyolites are according to Castillo, 2012; Defant & Drummond, 1990).

These geochemical features suggest they formed in an arc setting. Their Th/La and Nb/La ratios vary from 0.04 to 0.4 and 0.04–0.8, respectively.

4.3. The 50–35 Ma Magmatic Episode

The Eocene episode is widespread in all parts of the NE Iran BA and include GC plutonic and volcanic rocks, JC volcanic rocks, and KC igneous rocks. Plutonic rocks show two calc-alkaline and adakitic geochemical signatures. In the $K_2O + Na_2O$ versus SiO_2 diagram, GC intrusive rocks have monzogabbro to syenitic composition, whereas the KC intrusive rocks have granitic compositions, although some are syenite to monzodiorite-diorite (even gabbro) (Figure 5a). These rocks have high-K calc-alkaline to calc-alkaline signatures in the K_2O versus SiO_2 diagram (Figures 5c and 5d) and show high Th/Yb and Nb/Yb ratios and strong subduction zone signatures (Figures 6a and 6b). GC plutonic rocks have high Sr/Y (~65–139) ratios, similar to adakites (Figures 6c and 6d), while KC granitoids have low Sr/Y, similar to normal arc igneous rocks. GC plutonic rocks are strongly enriched in LREE relative to HREE (Figures 7c–7e) and are characterized by strong depletion in Nb, Ta, and Ti and enrichment in Cs, Rb, Ba, Th, and U relative to N-MORB. KC granitoids have LREE-enriched patterns ($La_{(n)}/Yb_{(n)} = 4.5–11.1$) and show slightly to highly negative Eu anomalies (Figure 7a), enrichment in Rb, Ba, K, U, Th, and Pb, and depletion in Nb, Ta, and Ti relative to MORB (Figure 7b).

Eocene BA volcanic rocks also have two different geochemical signatures. In the $K_2O + Na_2O$ versus SiO_2 diagram, GC volcanic rocks have trachy-andesitic to trachyte compositions (Figures 5a and 5b), whereas JC volcanic rocks have basaltic-andesite to rhyolite and trachybasaltic-andesite to trachyte compositions (Figure 5b). These samples show both medium- and high-K calc-alkaline signatures (Figure 5d). These volcanic rocks have variable Th/Yb ratio (0.3–14.5), similar to other arc-related rocks. In the Sr/Y versus Y diagram (Defant & Drummond, 1990), JC volcanic rocks display both normal calc-alkaline and adakitic signatures (Figure 6d). However, GC volcanic rocks also have higher Sr/Y (~65–139) ratio and are similar
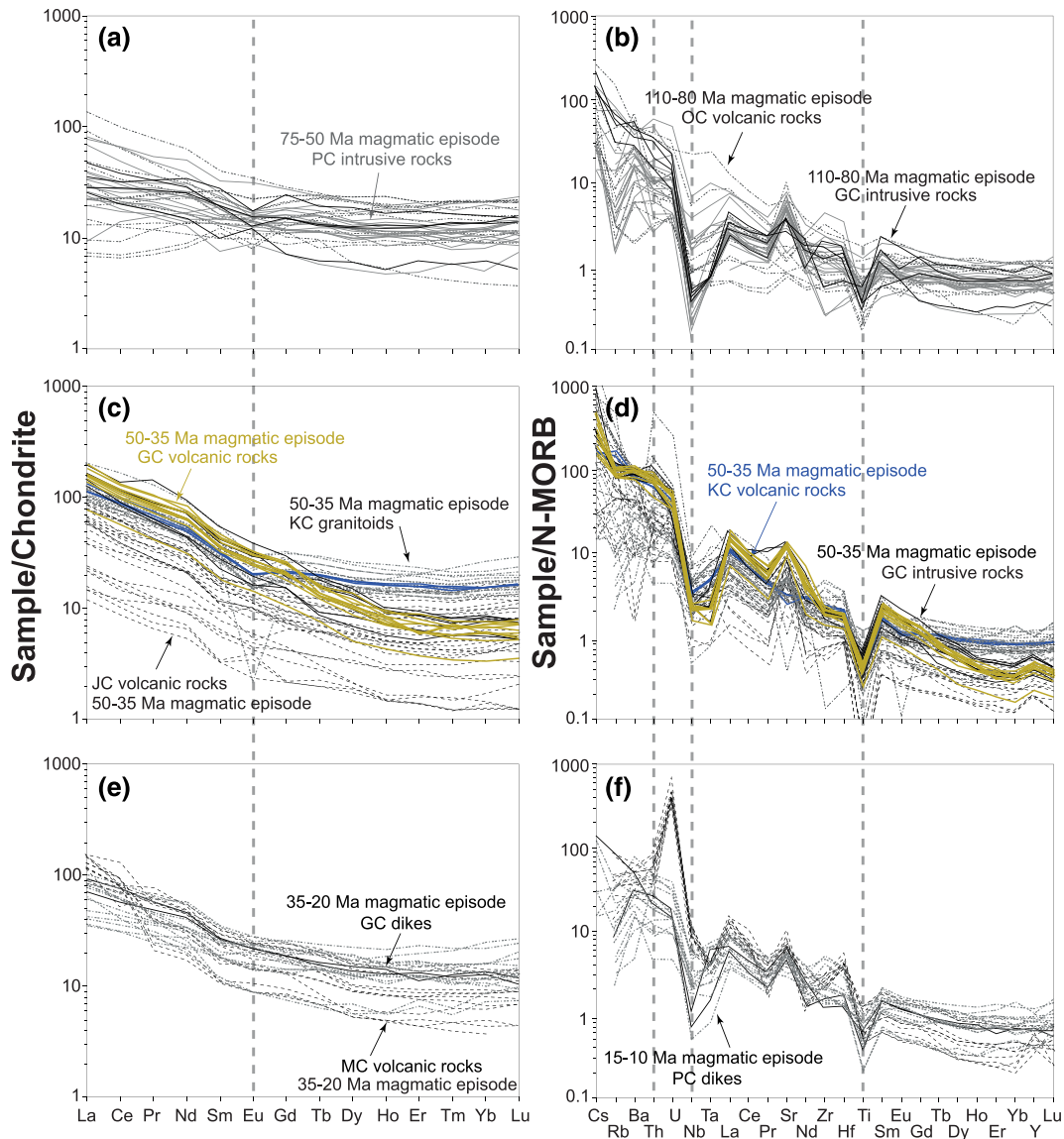
Figure 7. (a–f) Chondrite- and N-MORB-normalized REE and trace element patterns of NE Iran BA igneous rocks from different magmatic episodes. Normalization data are from Sun and McDonough (1989).

to adakites (Figures 6c and 6d). GC volcanic rocks show strong enrichment in LREE relative to HREE ($La_{(n)}$/$Yb_{(n)}$ ~ 18–29) (Figures 7c–7e) and are strongly depleted in Nb, Ta, and Ti relative to N-MORB (Figures 7d–7f). JC samples also show variable REE patterns (Figure 7c), with $La_{(n)}$/$Yb_{(n)}$ ranging from 1.2 to 24.4. These rocks are depleted in Ta, Nb, and Ti, but enriched in Rb, K, Sr, and Zr-Hf. KC volcanic rocks have trachyandesitic to dacitic compositions (Figure 5b), similar to high-K calc-alkaline series. These rocks are characterized by fractionated REE patterns ($La_{(n)}$/$Yb_{(n)}$ = 7.7–9.8), depletion in Nb-Ta-Ti, and enrichment in Rb, Ba, Th, U, K, and Pb (Figures 7e and 7f).

4.4. The 35–20 Ma Magmatic Episode

The Oligocene (plus latest Eocene and earliest Miocene) BA magmatic episode includes GC dikes and MC volcanic rocks. GC dikes are characterized by basaltic (SiO_2 = 49.9 wt.%) and trachy-andesitic (SiO_2 = 53.8 wt. %) compositions (Figure 5b). They have both calc-alkaline and high-K calc-alkaline signatures (Figure 5d). These dikes have high Th/Yb (1.2–1.5) and low Sr/Y (27.6–29.9) and are similar to normal arc-related rocks. Compared to N-MORB they are characterized by slight enrichment in LREE ($La_{(n)}$/
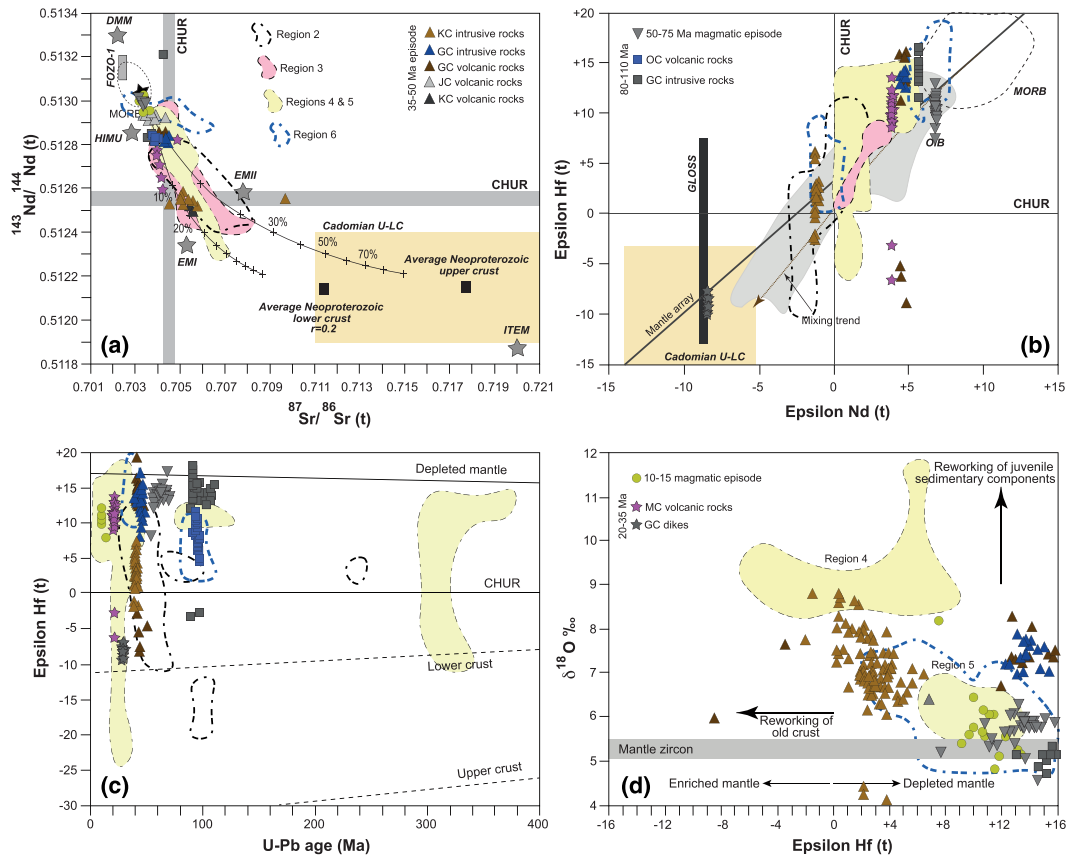
Figure 8. (a) $^{143}Nd/^{144}Nd$ versus $^{87}Sr/^{86}Sr$ for the NE Iran BA rocks compared with the mantle components HIMU, EMI, EMII, and DMM (Zindler & Hart, 1986); FOZO1 (Hart & Hauri, 1992), ITEM (Bell et al., 2004); and CHUR (Chondritic Uniform Reservoir). Data for the Cadomian upper and lower crust (U-LC) rocks are from Moghadam, Khademi, et al. (2015). Isotope data for NW and North Iran magmatic rocks (Regions 2 and 3) are from Aghazadeh et al. (2010), Aghazadeh et al. (2011), Asiabanha et al. (2009), Asiabanha and Foden, 2012, Castro et al. (2013), and Moghadam, Griffin, et al. (2017c). Data for the Urumieh-Dokhtar Magmatic Belt (Regions 4 and 5) are from Alavijeh et al. (2017) and Honarmand et al. (2013). The assimilation-fractional crystallization (AFC) is simulated based on the algorithm proposed by Ersoy & Palmer (2013). The composition of average Cadomian lower and upper crust is according to Moghadam, Khademi, et al. (2015). (b) εHf(t) versus εNd(t) for the NE Iran BA magmatic rocks. MORB and OIB data are from Chauvel and Blichert-Toft (2001), Nowell et al. (1998), Pearce et al. (1999), and Woodhead et al. (2001). Mantle array data are after Vervoort and Blichert-Toft (1999). (c, d) Epsilon Hf versus $^{206}Pb/^{238}U$ and $\delta^{18}O$ versus epsilon Hf plots for NE Iran RA zircons.

$Yb_{(n)} \sim 4.4–5.5$) (Figure 7e), negative anomalies in Nb, Ta, and Ti and positive anomalies in Rb, Ba, Th, and U (Figure 7f).

MC volcanic rocks show variable compositions in the $K_2O + Na_2O$ versus SiO_2 diagram (Figure 5b), ranging from trachy-basaltic andesite to andesite-dacite to trachyte (Ahmadi et al., 2017), but most are calc-alkaline (Figure 5d). These rocks have both low and high Th/Yb ratio, but Nb/Yb ratio is high in all rocks (Figure 6b). Their Sr/Y ratio is also low to high (~23–100) and show some adakitic tendencies (Figure 6d), including LREE enrichment ($La_{(n)}/Yb_{(n)} \sim 7.1–45.2$) (Figure 7e). Relative to N-MORB, they are characterized by Nb-Ta depletion and Th and U enrichment (Figure 7f).

4.5. The 15–10 Ma Magmatic Episode

The Middle Miocene magmatic episode includes Paybaz complex dikes. These have variable SiO_2 (47.3–70.5 wt.%), Al_2O_3 (~15.2–19.1 wt. %), K_2O (0.2–2.5 wt. %), and Mg# (7.1–41.9). Dikes have bimodal geochemical signatures, with rhyolite-trachyte and basalt-basaltic andesite to trachy-basaltic andesite compositions in the $K_2O + Na_2O$ versus SiO_2 diagram (Figure 5b). They mostly have low-K tholeiitic characteristics, although some samples show high-K calc-alkaline signatures (Figure 5d). They have variable Th/Yb ratios (0.2–4.5) and show similarities both to the subduction- and non-subduction-related rocks in the Th/Yb versus Nb/Yb diagram (Figure 6b). These rocks have moderate Sr (239–526 ppm) contents and Sr/Y ratios

(8.5–38.6), resembling normal arc rocks (Figure 6d). These rocks are variably enriched in LREE, with $La_{(n)}$/$Yb_{(n)} \sim 2.6$–10.3 (Figure 7c). They have positive anomalies in Ba, Th, U, and negative anomalies in Nb, Ta, and Ti relative to N-MORB (Figure 7d), similar to other arc rocks. Their Th/La and Nb/La ratios vary from 0.1 to 0.4 and 0.1–0.7.

5. Bulk-Rock Sr-Nd and Zircon Hf-O Isotopes

Isotopic compositions of NE Iran back-arc rocks are shown in Figure 8. We used both bulk rock Sr-Nd and zircon Hf-O isotopes to better reveal NE Iran BA isotopic compositions. The initial values of $^{87}Sr/^{86}Sr$ and $^{143}Nd/^{144}Nd$ were calculated using sample ages from zircon U-Pb ages or inferred from the ages of the nearby samples. Zircon $^{176}Hf/^{177}Hf(t)$ ratios (for each spot) were calculated from their U-Pb ages. Zircon has very low Lu/Hf ratio (~0.005), which makes it a good isotopic tracer for Hf isotopes. This mineral is also a useful for tracing long-term magmatic processes (Andersen et al., 2004; Hawkesworth & Kemp, 2006). We use "radiogenic" and/or "depleted" to describe high values of bulk rock εNd(t) and zircon εHf(t) (>+2). The term "enriched" is used for high values of Sr and/or O isotopes or for low values of bulk rock εNd(t) and zircon εHf(t) values. Below we explain the isotopic signature of each magmatic episode separately.

5.1. The 110–80 Ma Magmatic Episode

Late Cretaceous igneous rocks from the GC have initial $^{87}Sr/^{86}Sr$ ratios of 0.70365 and 0.70436 εNd(t); +5.8 to +13.4 (Table S7). A leucogranitic dike shows higher value of εNd(t) = +13.4. OC volcanic rocks also show depleted εNd(t) values, from +5.7 to +6.2 and enriched initial $^{87}Sr/^{86}Sr$ ratios (0.70387 and 0.70453). The GC zircons have high εHf(t) values; +18.1 to +11.8 ($av = +14.5$), except two spots with εHf(t) = −2.9 and −3.5. The higher values are similar to N-MORB-type mantle source (Figure 8b). These rocks have low $δ^{18}O$ values; +4.6‰ to +5.4‰, which are similar to mantle zircons. Igneous rocks from the OC have juvenile signatures with radiogenic εHf(t) values of +4.6 to +11.2 (Figure 8c).

5.2. The 75–50 Ma Magmatic Episode

The initial (55 Ma) $^{87}Sr/^{86}Sr$ ratio of magmatic rocks from this episode varies between 0.70344 and 0.70379 (Table S7). Their initial $^{143}Nd/^{144}Nd$ ratio shows a limited range between 0.51292 and 0.51294, consistent with εNd(t) of +7.1 to +7.3. Zircons have high εHf(t) values; +17.1 to +7.7 (except one point with εHf(t) = −5.1). Zircons from this magmatic episode have variable $δ^{18}O$, from +3.3‰ to +6.3‰.

5.3. The 50–35 Ma Magmatic Episode

Eocene igneous rocks from the GC have narrow range of initial $^{87}Sr/^{86}Sr$ (0.70457 and 0.70427) and εNd(t) (~ + 4 − +4.9). The JC rocks have $^{87}Sr/^{86}Sr$ ratio of 0.70446 to 0.70356 with εNd(t) varying between +6.1 and + 6.6. KC igneous rocks show a narrow range of $^{87}Sr/^{86}Sr$ ratios (0.70471 and 0.70587, except one aplitic dike with high ratio of 0.70974) and εNd(t) values (−0.4 to −2.3). The GC rocks have variable εHf(t) values of +19 to −8.3, but most zircons have depleted Hf isotopic composition (+19 to +8.1; $av = +13.8$). Zircons from these rocks have higher $δ^{18}O$, from +5.9‰ to +8.2‰. These zircons are from adakitic rocks associated with Cu mineralization. KC rocks have variable εHf(t) values, varying from +7.2 to −1.9 ($av = +2.8$). The Hf isotopic compositions of the KC rocks is less depleted and show considerable interaction with Cadomian crust (Figure 7c). Granitoids from the KC have variable $δ^{18}O$ values of +4‰ to +8.7‰ (with $av \sim 7‰$).

5.4. The 35–20 Ma Magmatic Episode

Andesitic dike from the GC is isotopically enriched with εNd(t) (−8.3) but with high initial $^{87}Sr/^{86}Sr$ (0.70447). Dacitic lavas from the MC have variable initial $^{87}Sr/^{86}Sr$ ratios (0.70409 and 0.70503) and εNd(t) (+4.04 to −0.58). Andesitic dike displays enriched εHf(t) values, from −7.1 to −9.4. The plot of zircon εHf(t) versus bulk rock εNd(t) suggests that this magma may have been generated from remelting upper crust (Figure 7b). The MC lavas display variable εHf(t) values, from +13.7 to +8.8, excluding two spots with εHf(t) of −3 and − 6.5.

5.5. The 15–10 Ma Magmatic Episode

The initial (12 Ma) $^{87}Sr/^{86}Sr$ ratio of the PC dikes varies between 0.70335 and 0.70367 (Table S7). Their εNd(t) values show a narrow range between +5.7 and +7.6. The Hf isotopic composition of dikes span a εHf(t) range

Table 2
Summary of Geochemical and Isotopic Characteristics of Different Magmatic Pulses From NE Iran

Magmatic pulse	Major and trace elements characteristics	Bulk rock and zircon isotopic signatures
110–80 Ma episode	Low-K tholeiitic to calc-alkaline and high-K calc-alkaline signatures. High to low Th/Yb and low Sr/Y ratios. Depletion and enrichment in LREE relative to HREE, depletion in Nb-Ta but enrichment in Rb, Ba, Th, and U.	Radiogenic bulk rock εNd(t) vlaues; +5.8 to +13.4 and +5.7 to +6.2. High zircon εHf(t) values; +18.1 to + 11.8 and +4.6 to 11.2 but low δ18O values; +4.6‰ to +5.4‰.
75–50 Ma episode	Mostly low-K tholeiitic with low to high Th/Yb but low Sr/Y ratios. Depletion and enrichment in LREE relative to HREE, depletion in Nb-Ta but enrichment in Th and U.	High bulk rock εNd(t) values of +7.1 to +7.3 and zircon εHf(t) values of +17.1 to + 7.7 but variable δ18O, changing from +3.3‰ to +6.3‰.
50–35 Ma episode	Calc-alkaline to high-K calc-alkaline with variable Sr/Y ratios; both high similar to adakites and low similar to normal arc rocks. High Th/Yb and mild to strong enrichment in LREE relative to HREE along with depletion in Nb-Ta-Ti and enrichment in Rb, Ba, Th, U, K, and Pb.	Radiogenic bulk rock εNd(t) values of +4 to +4.9 and +6.1 to 6.6. Some rocks have unradiogenic εNd(t) values of −0.4 to −2.3. Variable zircon εHf(t) values of +19 to +8.1 and +7.2 to −1.9 with δ18O values of +5.9‰ to +8.2‰ and +4‰ to +8.7‰.
35–20 Ma episode	Calc-alkaline to high-K calc-alkaline signatures with high to low Th/Yb, and Sr/Y ratios. Slight to strong enrichment in LREE compared to HREE, negative anomalies in Nb, Ta, Ti, and positive anomalies in Rb, Ba, Th, and U.	Andesitic dikes are unradiogenic with εNd(t) values of −8.3, but dacitic lavas show radiogenic εNd(t) values of +4.04 to −0.58. Intermediate dikes have less radiogenic εHf(t) values, changing from −7.1 to −9.4, whereas lavas have values of +13.7 to +8.8.
15–10 Ma episode	Low-K tholeiitic to high-K calc-alkaline with low to high Th/Yb but low Sr/Y ratios. Variable enrichment in LREEs with positive anomalies in Ba, Th, U, and negative anomalies in Nb, Ta, and Ti.	The εNd(t) value for dike changes between +5.7 and +7.6, with zircon εHf(t) values of +13.4 to +7.7 and δ18O values of +4.8‰ to +8.2‰.

of +13.4 to +7.7, showing melt derivation from depleted mantle (Figures 7b and 7c). The $\delta^{18}O$ varies from +4.8‰ to +8.2‰, similar to the mantle zircons with $\delta^{18}O$ of +5.3‰.

5.6. Summary of Geochemical-Isotopic Characteristics of NE Iran Back-Arc Magmatic Pulses

Zircon U-Pb ages indicate five magmatic episodes in the NE Iran BA: 110–80, 75–50, 50–35, 35–20 Ma, and 15–10 Ma. Each magmatic pulse seems to have its own geochemical signature, although some are similar. The geochemical and isotopic characteristics of different magmatic pulses from NE Iran are summarized in Table 2. Magmatic rocks from the first magmatic episode (110–80 Ma) have low-K tholeiitic to calc-alkaline affinities and show weak to strong subduction-related geochemical signatures. They have low Sr/Y ratios and are nonadakitic. Radiogenic bulk rock Nd and zircon Hf-O isotopes show that these magmas came from melting of a depleted source. The next episode (75–50 Ma) was also characterized by low-K tholeiitic rocks, showing variable subduction-related geochemical signatures; these are also nonadakitic. Similar to the first episode, magmatic rocks from 75–50 Ma episode show depleted bulk rock Nd and zircon Hf isotopes, indicating a depleted mantle source. Magmatic rocks from the 50–35 Ma episode show strong subduction-related signatures (enrichment in LREEs and strong depletion in Nb-Ta with high Th/Yb ratio) and have both high and low Sr/Y ratios. The isotopic ratios of these rocks are variable and change from depleted to enriched Nd and Hf; although zircon O isotopes extend to higher values.

The 35–20 Ma magmatic rocks are geochemically and isotopically variable, show both slight to strong subduction-related geochemical signatures, and vary from isotopically depleted to highly enriched rocks. Magmatic rocks from the 15–10 Ma episode show variable geochemical signatures (low-K tholeiitic to high-K calc-alkaline with low to high Th/Yb). All of the igneous rocks show high bulk rock Nd and zircon Hf isotopic ratios, indicating a variably metasomatized depleted mantle source for the formation of these magmas.

6. Discussion

In this section we discuss our results and combine these with published data to address three issues: (1) What was the timing of Iran BA magmatic pulses and how do these compare with those of the MF? (2) How did BA magmas form and evolve? And (3) what was responsible for the observed pulses of MF and BA arc magmatism in Iran?

6.1. Timing of Iran Back-Arc Magmatic Pulses

Zircon U-Pb ages indicate that NE Iran BA magmatic episodes occurred at 110–80, 75–50, 50–35, 35–20, and 15–10 Ma (Figure 1c). For identifying each pulse, we assume that there is a simple relationship between the volume of magma generated per arc length for each time and the number of dated samples. Therefore, the age peaks shown in Figures 1c–1e are interpreted as being proportional to magmatic flux. To further test this, we calculated the magmatic addition rate (Paterson et al., 2011; Paterson & Ducea, 2015). The magmatic addition rate is an estimate of total volume of magma added to an arc per unit of time. This rate is expressed in units of volume (km^3) per kilometer of arc length per unit of time and is expressed in as km^3/million years-km) (Ducea & Barton, 2007).

Considering a continental crust ~35–40 km thick (which is consistent with the presumed Moho depth in Iran MF and BA obtained from seismic data; e.g., Entezar-Saadat et al., 2017; Mottaghi et al., 2013; Verges et al., 2011) and using the exposed area for igneous rocks of each magmatic pulse, the apparent magma addition rates are 80 ± 15 km^3/Myr-km for the 110–80 Ma magmatic episode, decreasing to ~20 ± 5 km^3/Myr-km for the 75–50 Ma magmatic pulse, and increasing to ~200 ± 50 km^3/Myr-km during the 50–35 Ma magmatic flare-up. Younger magmatic pulses show; 15 ± 5 km^3/ Myr-km for the 35–20 Ma pulse and 30 ± 5 km^3/ Myr-km for the 15–10 Ma episode. The flare-up at 50–35 Ma increases to ~220 ± 40 km^3/Myr-km toward the NNW Iran BA. It is noteworthy that the 50–35 Ma pulse the MF is also dominant, with a maximum estimate of ~250 ± 50 km^3/Myr-km arc length.

The first magmatic episode (110–80 Ma) corresponds to a time of strong regional extension due to subduction initiation along what is now the Zagros suture zone (Moghadam & Stern, 2011), whereas younger episodes mark the operation of first a mature subduction zone during Paleogene and then collision-related magmatism during Neogene (Deevsalar et al., 2017; Kheirkhah et al., 2015; Neill et al., 2015). During the first magmatic episode, several oceanic back-arc basins opened, including the Sabzevar ophiolites of NE Iran (Moghadam et al., 2013; Moghadam et al., 2014), but this magma production is not included in our estimated magmatic flux. Back-arc basin formation was concomitant with faulting, uplift and core complex exhumation in parts of the Iranian plateau (Malekpour-Alamdari et al., 2017; Moritz et al., 2006; Verdel et al., 2007). Back-arc plutonism intensified between 105 and 90 Ma, as also suggested by Alaminia et al. (2013). Intrusive rocks from this episode have calc-alkaline characteristics whereas most extrusive rocks have MORB-like geochemical signatures. Intrusive rocks appear to be derived from depleted, MORB-like mantle with depleted Hf but less depleted Nd isotopes. The melts responsible for this magmatic episode are relatively uncontaminated by continental crust (Figures 8 and 9). εHf(t) values for the extrusive rocks suggest derivation from enriched lithospheric mantle. From ~80 to 75 Ma there was greatly reduced magmatism. The end of the 80–75 Ma lull was associated with exhumation of the Sabzevar ophiolite complex, which was then buried beneath early Paleocene conglomerates and other detritus containing abundant ophiolite fragments (Moghadam et al., 2014; Tadayon et al., 2018). This is also confirmed by low-temperature thermochronometric and structural evidence, which show that ophiolite uplift was accompanied by dextral transpression beginning in early Paleocene (~70–60 Ma) and ending in the Miocene-Pliocene (5 Ma) (Tadayon et al., 2018). Another magmatic pulse started at 75 Ma and lasted until 50 Ma (early Eocene). These igneous rocks are mostly low-K tholeiites to calc-alkaline and nondakitic in composition as shown by low Sr/Y and La$_{(n)}$/
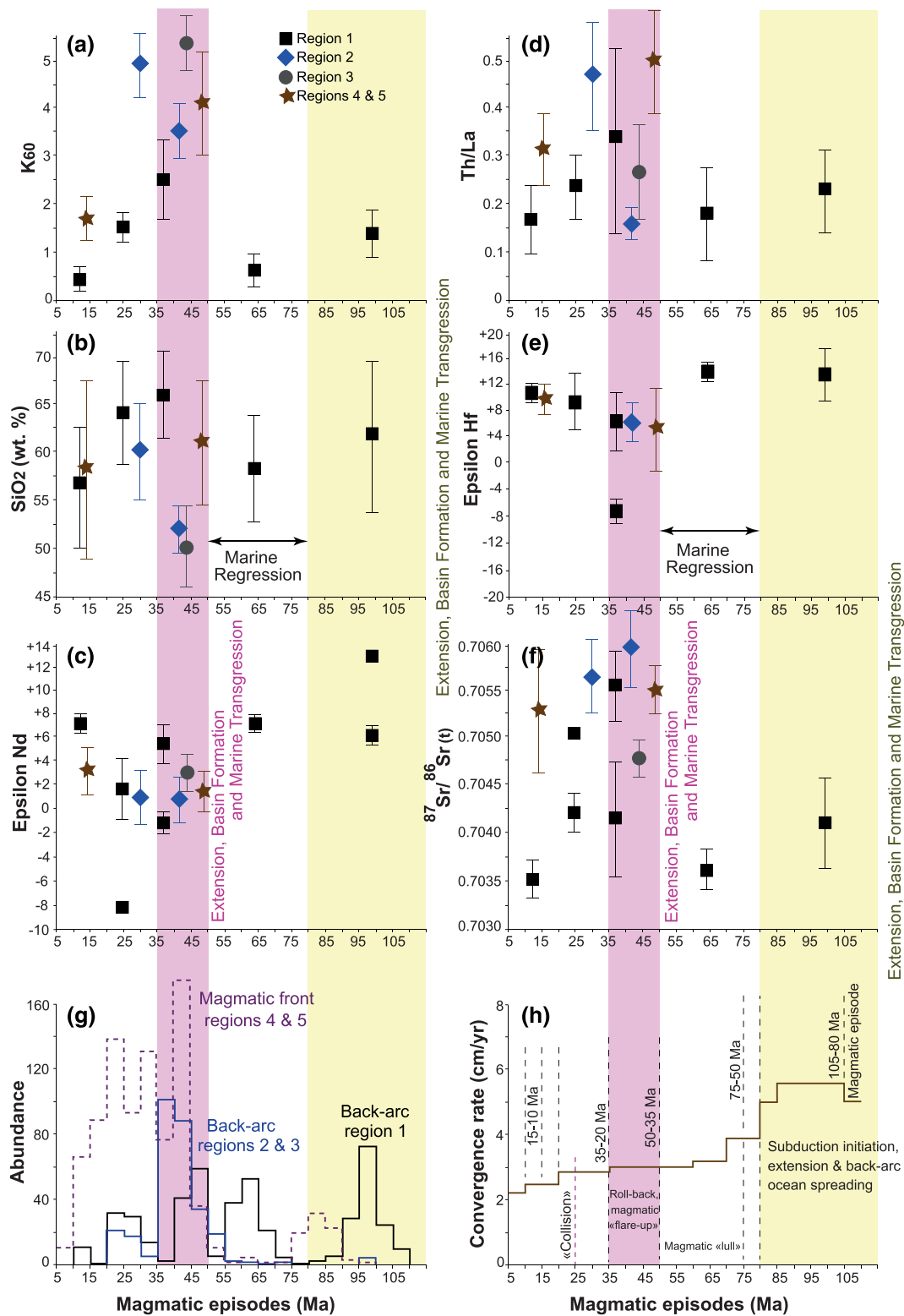
Figure 9. Compositional variations of K_{60} (potash content at 60 wt.% SiO_2, recalculated to 100% anhydrous) (a), SiO_2 (b), whole rock $\varepsilon Nd(t)$ (c), Th/La (d), zircon $\varepsilon Hf(t)$ (e), and $^{87}Sr/^{86}Sr$ (F) for different magmatic pulses of the NE Iran BA. (g, h) The age distribution for Iran MF and BA magmatism (based on new and compiled zircon U-Pb age data) and their relationships with the Arabia-Iran (Eurasia) convergence rate during late Early Cretaceous (110 Ma) to present (adapted from McQuarrie & van Hinsbergen, 2013; Agard et al., 2007). For comparison, we also show episodes of extension, basin formation, sea level regression, and transgression.

$Yb_{(n)}$ ratios. Both bulk rock Nd and zircon Hf-O isotopes show that these magmas were dominated by mantle inputs. The Eocene magmatic pulse (50–35 Ma) includes both high K calc-alkaline rocks and high to low Sr/Y magmas. These magmas are isotopically variable, from highly depleted (Nd and Hf) adakitic rocks to nonadakitic and isotopically enriched rocks showing more crustal input. Eocene magmatism was associated with strong extension in the Iranian plateau, including exhumation of core complexes (Verdel et al., 2007).

The 35–20 Ma magmatic pulse was characterized by calc-alkaline, highly contaminated and/or crustally-derived (with negative bulk rock $\varepsilon Nd(t)$ and zircon $\varepsilon Hf(t)$ values) rocks. The youngest magmatic pulse at 15–10 Ma was nonadakitic and dominated by mantle inputs. This is a minor pulse in NE Iran BA, and mostly occurs as dikes. These dikes contain significantly older zircons, reflecting recycling of some older continental crust.

New zircon U-Pb data presented in this study indicate that the entire NE Iran BA region was affected by ~100 Myr of pulsed magmatism. The 50–35 Ma magmatic episode likely triggered hydrothermal circulation, which may have helped form minor porphyry Cu deposits. A middle Eocene episode of hydrothermal alteration is supported by ages of biotite from potassic alteration zones around monzogabbroic stocks and amphibole from trachyandesites, which yield ^{40}Ar-^{39}Ar ages of 43.7 ± 0.1 and 42.7 ± 0.2 Ma, respectively. The Cu mineralizing event in NE Iran BA is attributed to the middle Eocene episode, which agrees with occurrence of high Sr/Y rocks and the narrow range of zircon U-Pb and Ar-Ar ages for rocks of this episode.

The new age data from NE Iran BA rocks and compiled ages for both BA rocks from N-NW and MF (UDMB) rocks show some differences. Back-arc magmatism from N-NW Iran lacks evidence for a significant 110–80 and 75–50 Ma magmatic episode but instead shows major 55–35 and 35–20 Ma pulses. Data from the MF display two main episodes at 95–75 and 55–5 Ma, indicating more continuous magmatism.

6.2. Source and Evolution of Iran Back-Arc Magmas

Not all arcs have BA igneous activity, but those that do show distinct compositional variations from MF to BA (Kuno, 1966). The across-arc compositional variations for global convergent margins was suggested to reflect increasing depth to the subduction zone (Dickinson & Hatherton, 1967); this relationship is thought to reflect different compositions of fluids released from the subducted slab between those at ~100 km beneath the MF and those released deeper beneath the BA. However, these conclusions do not hold true for all arcs worldwide (Chapman et al., 2017; Heydolph et al., 2012a; Hochstaedter et al., 2001). It is also thought that arc magma compositions evolve over 10 to 100 Ma timescales, from older arc tholeiites to younger calc-alkaline suites and, in some cases, to very mature alkalic suites such as shoshonites (Jakes & White, 1969). The question of whether the composition of arc magmas changes with time has not been considered for BA magmatism in general or Iran BA magmatism in particular. The ~90 Myr magmatic history of the Iran BA makes this a good place to evaluate whether or not these magmas change in composition systematically with time, and what are the controls.

To understand the magmatic evolution of Iran rear-arc magmatism, we used potash content (recalculated to 100% anhydrous) of rocks from different magmatic pulses at 60 wt.% SiO_2. This parameter is known as K_{60} and is thought to reflect depth to the subducted slab (Dickinson & Hatherton, 1967). Figure 9a captures the temporal evolution of the Iranian BA as reflected in the mean compositions of the five magmatic episodes we have described. K_{60} values are low (<1.5 wt. % for the two early episodes (110–80 and 75–50 Ma) then jumps to >1.5 wt. % for the next two (Paleogene) episodes (50–35 and 35–20)). The K_{60} values of the 110–80 Ma episode suggests a depth to the Benioff zone beneath the volcanos (h) of ~115 ± 5 km. This value changes to 90 ± 10 km (h) for the 75–50 Ma magmatic episode. During the 50–35 Ma magmatic pulse, h increased to 210 ± 50 km. For the 35–20 Ma magmatic pulse, the slab seems to have shallowed to 120 ± 15 km. However, these estimated depths may be too great for especially the 50–35 Ma and 35–20 Ma episodes. These magmatic rocks are contaminated by interaction with continental crust (see next explanation), and it is not clear how much K and Si is due to such contamination.

Iran BA magmatic pulses also capture changes from mafic to felsic with time (Figure 9b). However, the 50–35 Ma flare-up erupted abundant basalt interspersed with silicic counterparts. Both have similar isotopic signatures and can be explained due to high extension rates and thin crust of the Iran BA, allowing basaltic melts to more easily rise to the surface. This effect is more conspicuous for igneous rocks of the Iran MF (Figure 9b). However, 50–35 Ma magmatic rocks contain zircons with a wide range of epsilon Hf

(~−8 to ~+19). Our Iran BA bulk rock Nd and zircon Hf isotopic data indicate greater involvement of continental crust and/or lithosphere with time (Figures 9c–9e). Variations in the Th/La ratio (Figure 9d) also support this interpretation. The lower continental crust beneath the Iran BA may have been where MASH (melting, assimilation, storage, and homogenization) processes and formation of 50–35 Ma adakitic magmas occurred. We see no evidence that these adakitic magmas were produced by melting of subducted oceanic crust; instead, their generation is better explained by partial melting of lower crust in an environment where amphibole (±garnet) were residual or fractionating phases (e.g., Davidson et al., 2007). The MASH mechanism is especially useful for forming JC (Region 1d) adakites (Moghadam, Li, et al., 2016).

Compiled isotopic data reveals that zircon εHf(t) bulk rock εNd(t) for magmatic rocks are variable for 50–35 and 35–20 Ma BA pulses but are less variable for earlier (110–80 and 75–50 Ma) pulses. It is widely accepted that the radiogenic isotopic composition of continental arc rocks is more evolved during flare-up events, a temporal change, which is known as isotopic pull-down (Chapman & Ducea, 2019). Isotopic pull-down during flare-ups can have different causes including (a) underthrusting and melting of continental lower crust and mantle into the melt source region, (b) incorporation of lithospheric mantle with different age and isotopic composition, (c) differing extents of continental crust assimilation, and (d) changes in the isotopic composition of assimilated materials.

Involvement of mantle lithosphere and/or asthenosphere may control zircon Hf and bulk rock Nd isotopic compositions of magmatic rocks for some magmatic episodes. For example, more juvenile radiogenic isotopes for magmatic rocks suggest thinning or partial removal of mantle lithosphere with melting of asthenosphere to generate isotopically depleted magmas of the 75–50 Ma episode and probably oceanic mantle lithosphere for magmas of the 110–80 Ma pulse. On the other hand, assimilation of continental crust also plays another major role especially for 50–35 Ma magmatic episode. Melting of a metasomatized mantle above the subduction zone will increase the content of incompatible elements such as Th, U, and K, which is indistinguishable from continental crust contamination. Melting of a metasomatized mantle wedge (contaminated by slab components) can also affect the isotopic compositions of arc lavas, but the changes are not comparable with assimilation of continental crust. We believe that the AFC processes can influencing the isotopic composition of the fractionated rocks from NE Iran BA, as there are sufficient isotopic contrasts between Paleogene magmas and Iran Cadomian old crust.

To discriminate between a metasomatized mantle source (or even asthenosphere) and AFC processes for the generation and evolution of each magmatic pulses from NE Iran BA, we used zircon δ^{18}O versus bulk rock ^{87}Sr/^{86}Sr, zircon εNd(t), and bulk rock εNd(t) versus SiO$_2$ (Figure 10) plots. Oxygen isotopes are useful, as there is a large variation between the O isotopic composition of mantle and crustal rocks. This, when combined by radiogenic isotopes (such as Sr), can be used effectively for discriminating between source (metasomatized mantle) and crustal (continental crust with AFC-dominated processes) contamination (Davidson et al., 1990; Davidson et al., 2005).

Magmatic rocks from 110–80, 75–50, and 15–10 Ma show mantle-like isotopic characteristics and the small-degree isotopic variations among them can be ascribed to the different isotopic fertility of their mantle sources. Correlations between bulk rock Sr isotopic ratios and zircon oxygen isotopes (Figure 10a) argue strongly for crustal contamination for 50–35 Ma magmatic episode rocks. Bulk rock Nd and zircon Hf isotopic compositions plotted against SiO$_2$ content also support an AFC mechanism for the evolution of 50–35 and 35–25 Ma magmatic episode rocks (Figures 10b and 10c). This argues that the Nd and Hf isotopic composition (as well as O and Sr) is modified by crustal contamination occurring simultaneously with fractional crystallization, which increases SiO$_2$ content. In contrast, both intermediate and acidic magmatic rocks from 110–80 and 75–50 Ma magmatic pulses have similar isotopic signatures and seem to not have been affected by AFC processes. In contrast, the isotopic differences between OC and GC Late Cretaceous rocks (Figure 10b) can reflect changing isotopic compositions of the mantle source.

6.3. Magmatic Triggers and Arc Tempos in Iran MF and BA

Late Mesozoic-Cenozoic magmatism in Iran varied as this region cycled between extension and contraction (Figures 11a–11c), with the most voluminous magmatism associated with and probably triggered by extension. We suggest that the high magmatic fluxes during Late Cretaceous (110–80 Ma) and Eocene (50–35 Ma)
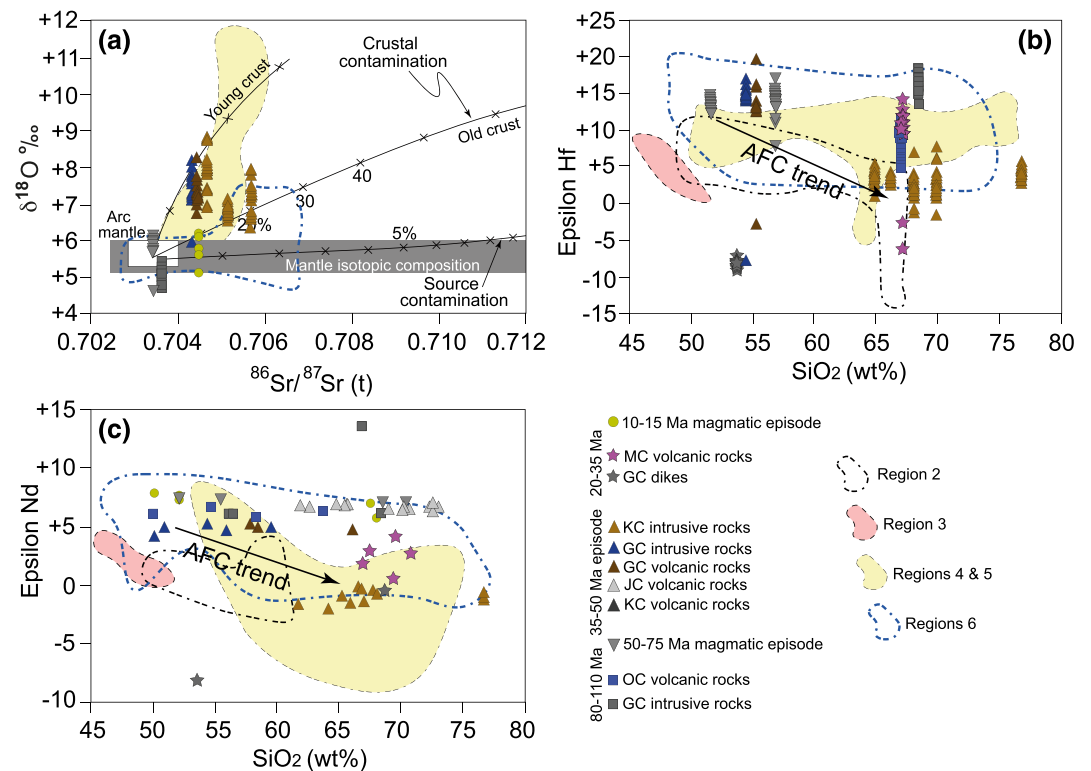
Figure 10. The $\delta^{18}O$ versus $^{87}Sr/^{86}Sr$ (a), zircon εHf versus SiO_2 (b), and bulk rock εNd(t) versus SiO_2 plots demonstrate the utility of zircon $\delta^{18}O$ and radiogenic isotopes as well as fractionation index (SiO_2) as unique indicators of crustal contamination in the NE Iran BA magmatic rocks. Panel (a) is modified after Davidson et al. (2005). References for compiled data are the same as in Figure 8.

reflect extensional episodes and that magmatic lulls during Latest Cretaceous to Early Eocene (75–50 Ma) and Latest Eocene to Miocene (35–20 and 15–10 Ma) correlate with compressional episodes.

There are several presumed triggers for the flare-up and lull episodes in Iran including changing subduction rates, changing subduction angles, and back-arc basin opening (e.g., (Verdel et al., 2011a).

6.3.1. Widespread Extension and Back-Arc Rifting

Kazmin et al. (1986) and Dercourt et al. (1986) suggested that Late Cretaceous and Eocene magmatism in Iran was related to the opening of back-arc basins, which need extreme extension. We believe that Late Cretaceous-Paleogene arc magmatism in Iran accompanied strong extension and lithospheric thinning— in the overlying plate of the subduction system- including in the BA environment. In fact, Paleogene Iran may be considered as a type example of an extensional continental convergent margin. Lithospheric extension is likely to lead to further weakening induced by upwelling of hot asthenosphere, and this will help further rifting of the convergent margin (DeCelles et al., 2009; Ducea et al., 2015a; Ferrari et al., 2013; Seebeck et al., 2014). Convergent margin rifting can be caused by trench retreat, slab roll-back, and steepening, slab tearing, or lithospheric delamination. We suggest that extension in the Iranian plateau triggered both lithospheric and asthenosphere mantle upwelling beneath the BA and generated different types of magmas (Sepidbar et al., 2019); but the asthenosphere mantle contributed extensively to the genesis of Late Cretaceous magmatic rocks, because these rocks have more juvenile or depleted isotopic signatures. In other hand, Eocene extension and crustal thinning was accompanied by decompression melting of the preexisting mantle wedge as well as incorporating underlying upwelling asthenosphere.

Much of the extension was associated with Late Cretaceous subduction initiation and then reactivated by slab roll-back during the Eocene (Moghadam et al., 2018; Moghadam & Stern, 2011) (Figures 11a–11c). We believe that the extensional phases—in the overlying plate of Neotethyan subduction zone—were accompanied by rifting of the Iranian plateau, which intensified BA magmatism. Deep sedimentary basins, some with true oceanic crust, were widespread across Iran during Late Cretaceous and Eocene times.
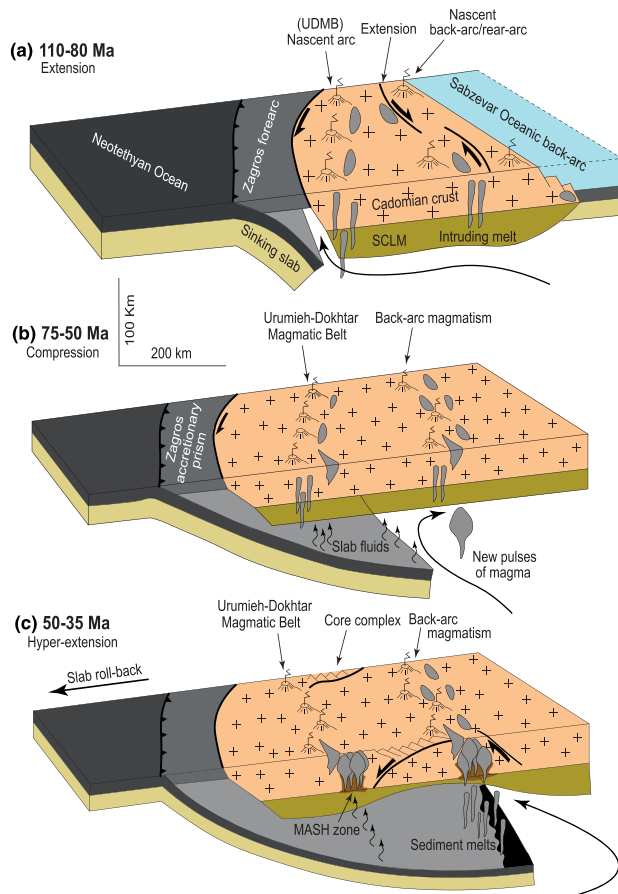
Figure 11. (a–c) Simplified cross section of the Late Cretaceous-Paleogene convergent margin of Iran, showing different magmatic pulses at 110–80, 75–50, and 50–35 Ma in the NE Iran back-arc magmatic belt. These panels emphasize the positions of the magmatic front (MF) and backarc (BA); slab fluids triggering MF magmatism versus sediment melts triggering BA magmatism, Subcontinental Lithospheric Mantle (SCLM), and Melting-Assimilation-Storage-Homogenization (MASH) processes beneath both MF and BA. Small wavy red lines show the trajectory of slab fluids whereas continuous red lines in (a)–(c) show asthenospheric mantle flow.

Although extensional versus compressional regimes within the Iranian plateau were accompanied by magmatic flare-up and lulls, respectively, there are other independent evidences for extensional and compressional phases in Iran. A synthesis of sea level changes in Iran and surrounding areas (e.g., Haq & Al-Qahtani, 2005; Rivandi et al., 2013) indicates that extensional phases were accompanied by marine transgression and deposition of thick (500–1000 m) sequences of deep marine *Foraminifera-* (Late Cretaceous) and *Nummulites* (Eocene)-bearing limestones, whereas compressional phases were followed by marine regression, uplift, erosion, and deposition of red volcano-sedimentary sequences. In both Late Cretaceous and Eocene outcrops in NE Iran, the presence of shallow to deep marine sediments interbedded with magmatic rocks can also be used as evidence for an extensional basin (Berberian & King, 1981; Verdel et al., 2011a) (Figures 9g and 9h). Core complexes are also evidence of extension, which were abundant during Late Cretaceous (110–80 Ma) and Eocene (50–35 Ma). Moreover, the stratigraphic records for Eocene subsidence in north and central Iran have been interpreted in terms of Eocene extension (Berberian & King, 1981; Brunet et al., 2003; Verdel et al., 2011a; Vincent et al., 2005). Eocene crustal thinning in the UDMB could also have caused drips or delamination in which the mantle lithosphere-lower crust was removed (e.g., (Pang et al., 2013).

6.3.2. Change in Subduction Angle

In addition to the role of upper plate compression or extension, the dip of the subducting slab can influence the distribution of BA magmatism. Simulation of the subduction processes suggests that prolonged subduction is not steady state and instead may be associated with cyclic shallowing and steepening of slab dip (Kay & Coira, 2009). Steeping slab dip favors roll-back and upper plate extension whereas shallowing slab dip stimulates upper plate compression. Slab rollback plays an important role during the life cycle of most arcs and can cause lithospheric thinning and rupturing to generate back-arc extension and eruption of juvenile magmas (Ducea et al., 2017). Paleogene extension of Iran is likely to have been related to subduction of old oceanic lithosphere, which favors roll-back. Furthermore, the interaction between the subducting lithosphere and the mantle transition zone for the old Tethyan slab could have increased the slab-pull forces, which triggered slab steepening and accelerated roll-back, as was proposed for magmatic flare-up in the Patagonian Andes (e.g., Iannelli et al., 2018; Paz et al., 2019).

The change in slab dip from Late Cretaceous to present could also control the spatial occurrence of magmatic rocks. These phenomena in close association with other triggers such as rifting in the BA due to extreme extension will control the extent of igneous activity. We, therefore, propose that Cenozoic extension may have been related to the steepening of the Neotethyan slab leading to trench roll-back (Figure 11c).

6.3.3. Change in Subduction Rate

Another possible explanation for arc magmatic flare-ups is increased rate of plate convergence. Increased flux of slab-derived fluids is expected if subduction velocity increases. In this scenario, increased hydrous flux will lead to increased partial melting and will produce high-volume of magmas. Positive correlations between increased convergence rate and flare-ups have been observed in some arcs (e.g., Huang & Lundstrom, 2007), although other studies show magmatic flare-ups coincide with low and/or decreasing convergence rates (e.g., Shellnutt et al., 2014) or show no obvious correlation (Ducea et al., 2015b; Zhang et al., 2019). Estimated convergence velocities between Arabia and Eurasia during the period 110–70 Ma (Agard et al., 2007) and 50–0 Ma (McQuarrie & van Hinsbergen, 2013) indicate that the 110–80 Ma magmatic flare-up occurred at relatively high convergence rate and with high obliquity (Figures 9g and 9h), whereas

the magmatic lull at 75–50 Ma was simultaneous with a low convergence rate. On the other hand, the younger magmatic flare-up at 50–35 Ma was accompanied by lower and decreasing convergence rate (Figures 9g and 9h). Finally, we think a combination of temporal change in subduction angle and the resultant widespread extension and back-arc basin rifting can better explain the magmatic flare-up in Late Cretaceous-Paleogene arcs of Iran.

6.3.4. Magmatic Lulls at 75–50 and 35–20 Ma

The Paleogene magmatic lull in Iran is suggested to be related to flat slab subduction (e.g., (Berberian & King, 1981). Flat subduction is accompanied by compression in the overlying plate. However, the magmatic lull during 75–50 Ma—after the flare-up at 110–80 Ma—can be related to subduction of an oceanic ridge (e.g., Agard et al., 2007) and/or a oceanic plateau (e.g., Bonnet et al., 2019). This magmatic lull was accompanied with ophiolite exhumation and erosion in Iran MF and BA. Recent syntheses for arcs worldwide including the Andes, suggest that after ridge or seamount subduction a period of slow subduction with lull magmatism occurs until the slab-pull forces restored (e.g., Iannelli et al., 2018; Paz et al., 2019). The magmatic lull at 35–20 Ma (and even 15–10 Ma) is probably related to the onset of continental collision between Iran and Arabia followed by slab detachment in Miocene.

6.3.5. Comparison With Other Arcs

The Late Mesozoic to Cenozoic Iran arc can be usefully compared with Andean-type convergent margins. In the Andes scenario, subduction of the oceanic slab causes mantle melting, and the ascending melts interact with the continental crust under compression to create both MF and BA magmatism. The Iranian example differs due to the strong extension that it experienced. This extension was accompanied by magmatism that further weakened the lithosphere and crust. The Andean arc is built on thick continental crust under a compressional tectonic regime, and the arc crust continues to shorten and thicken. Convergent margin magmatic systems are likely to show significant differences between compressional and extensional arcs. In compressional arcs, BA magmatic rocks are mostly restricted to ~200–300 km from the trench (~100–200 from the MF). In extensional convergent margins, back-arc magmatism can occur farther from the trench. For example, in the Izu-Bonin-Mariana arc, BA igneous activity happens as back-arc basin seafloor spreading but also as isolated volcanoes restricted to 150–200 km from the MF (Kodaira et al., 2010). In the western U.S. continental arc, which in Oligocene time was strongly extensional, back-arc magmatism occurs ~1000 km far from trench (e.g., the Oligocene San Juan Volcanic Field, USA) (Bachmann et al., 2002; Lake & Farmer, 2015). In eastern China, back-arc alkali basalts erupt hundreds of kilometers behind the MF in Japan (Kimura et al., 2018). Certainly, the distance of the BA from the MF in extensional arcs like Paleogene Iran partly reflected the dip of the subducting Neotethyan slab. Furthermore, the Andes convergent margin subduct young buoyant lithosphere and is compressional, whereas subduction of old Neotethyan lithospehere beneath Iran was responsible for Late Cretaceous-Paleogene extension and magmatic flare-ups.

7. Conclusions

Our multiscale investigation reveals that the NE Iran BA preserves a record of several magmatic pulses over ~100 Myr. Each magmatic pulse was characterized by distinct geochemical-isotopic signatures. We conclude the following six key points:

1. An extensional tectonic regime prevailed for Iran during the Late Cretaceous, due to subduction initiation along the Zagros trench. This extension led to back-arc opening and magmatism across NE Iran. Magmatic rocks from this episode are isotopically depleted and formed from melting of both depleted mantle and continental lithospheric mantle.
2. A second magmatic pulse at 75–50 Ma reflected partial melting of depleted mantle. This episode was linked to the compression of Iran during latest Cretaceous to Paleocene.
3. The next magmatic pulse at 50–35 Ma was characterized by an ~15 Myr magmatic flare-up, which is in accordance with high-magmatic fluxes across Iran at that time. During this episode, crustal MASH zones responsible for supplying magmas with crustal affinity, with enriched Nd-Hf and elevated O-Sr isotope signatures.
4. Two magmatic episodes at 35–20 and 15–10 Ma are also recorded in the NE Iran BA, but these were subordinate to earlier magmatic pulses. Igneous rocks produced by these magmatic pulses are isotopically variable.

5. Magmatic flare-up and lull episodes in the NE Iran BA differ temporally from those of that Iran MF; the BA flare-up occurred at 110–80 and 55–35 Ma, whereas MF burst happened at 95–75 and 55–5 Ma. Furthermore, the systematic geochemical variations from MF to BA documented for other continental arcs such as the Andes are not visible in the Iran convergent margin.

6. The observations of NE Iran BA igneous rocks provide a basis for understanding the evolution of magmatic processes in continental arcs, which are under extension and built on thin continental crust where tectonic and magmatic feedbacks are temporally and spatially different from those controlling better known continental arcs under compression.

References

Agard, P., Jolivet, L., Vrielynck, B., Burov, E., & Monie, P. (2007). Plate acceleration: The obduction trigger? *Earth and Planetary Science Letters*, *258*(3–4), 428–441.

Aghazadeh, M., Castro, A., Badrzadeh, Z., & Vogt, K. (2011). Post-collisional polycyclic plutonism from the Zagros hinterland: The Shaivar Dagh plutonic complex, Alborz belt, Iran. *Geological Magazine*, *148*(5–6), 980–1008.

Aghazadeh, M., Castro, A., Omran, N., Emami, M., Moinvaziri, H., & Badrzadeh, Z. (2010). The gabbro (shoshonitic)-monzonite--granodiorite association of Khankandi pluton, Alborz Mountains, NW Iran. *Journal of Asian Earth Sciences*, *38*(5), 199–219. https://doi.org/10.1016/j.jseaes.2010.01.002

Ahmadi, P., Ghorbani, M. R., Coltorti, M., Kuritani, T., Cai, Y., Fioretti, A. M., et al. (2017). High-Nb hawaiite–mugearite and high-Mg calc-alkaline lavas from northeastern Iran: Oligo-Miocene melts from modified mantle wedge. *International Geology Review*, *61*(2), 150–174.

Alaminia, Z., Karimpour, M. H., Homam, S. M., & Finger, F. (2013). The magmatic record in the Arghash region (northeast Iran) and tectonic implications. *International Journal of Earth Sciences*, *102*(6), 1603–1625. https://doi.org/10.1007/s00531-013-0897-1

Alavijeh, B. S., Rashidnejad-Omran, N., & Corfu, F. (2017). Zircon U-Pb ages and emplacement history of the Nodoushan plutonic complex in the central Urumieh-Dokhtar magmatic belt, Central Iran: Product of Neotethyan subduction during the Paleogene. *Journal of Asian Earth Sciences*, *143*, 283–295. https://doi.org/10.1016/j.jseaes.2017.03.034

Ali, S. A., Buckman, S., Aswad, K. J., Jones, B. G., Ismail, S. A., & Nutman, A. P. (2013). The tectonic evolution of a Neo-Tethyan (EoceneOligocene) island-arc (Walash and Naopurdan groups) in the Kurdistan region of the Northeast Iraqi Zagros Suture Zone. *Island Arc*, *22*(1), 104–125. https://doi.org/10.1111/iar.12007

Alizadeh, E., Ghadami, G., Esmaeily, D., Ma, C., Lentz, D. R., Omrani, J., and Golmohammadi, A., 2017, Origin of 1.8 Ga zircons in Post Eocene mafic dikes in the Roshtkhar area, NE Iran: International Geology Review, p. 1–28.

Al-Lazki, A. I., Sandvol, E., Seber, D., Barazangi, M., Turkelli, N., & Mohamad, R. (2004). Pn tomographic imaging of mantle lid velocity and anisotropy at the junction of the Arabian, Eurasian and African plates. *Geophysical Journal International*, *158*(3), 1024–1040. https://doi.org/10.1111/j.1365-246x.2004.02355.x

Andersen, T., Griffin, W. L., Jackson, S. E., Knudsen, T. L., & Pearson, N. J. (2004). Mid-Proterozoic magmatic arc evolution at the southwest margin of the Baltic Shield. *Lithos*, *73*(3–4), 289–318. https://doi.org/10.1016/j.lithos.2003.12.011

Asiabanha, A., & Foden, J. (2012). Post-collisional transition from an extensional volcano-sedimentary basin to a continental arc in the Alborz Ranges, N-Iran. *Lithos*, *148*, 98–111. https://doi.org/10.1016/j.lithos.2012.05.014

Asiabanha, A., Ghasemi, H., & Meshkin, M. (2009). Paleogene continental-arc type volcanism in North Qazvin, North Iran: Facies analysis and geochemistry. *Neues Jahrbuch Fur Mineralogie-Abhandlungen*, *186*(2), 201–214.

Authemayou, C., Chardon, D., Bellier, O., Malekzadeh, Z., Shabanian, E., & Abbassi, M. R. (2006). Late Cenozoic partitioning of oblique plate convergence in the Zagros fold-and-thrust belt (Iran). *Tectonics*, *25*(3), n/a–n/a.

Azizi, H., & Jahangiri, A. (2008). Cretaceous subduction-related volcanism in the northern Sanandaj-Sirjan Zone, Iran. *Journal of Geodynamics*, *45*(4–5), 178–190. https://doi.org/10.1016/j.jog.2007.11.001

Azizi, H., Lucci, F., Stern, R. J., Hasannejad, S., & Asahara, Y. (2018). The Late Jurassic Panjeh submarine volcano in the northern Sanandaj-Sirjan Zone, northwest Iran: Mantle plume or active margin? *Lithos*, *308-309*, 364–380. https://doi.org/10.1016/j.lithos.2018.03.019

Azizi, H., & Stern, R. J. (2019). Jurassic igneous rocks of the central Sanandaj–Sirjan zone (Iran) mark a propagating continental rift, not a magmatic arc. *Terra Nova*, *31*(5), 415–423. https://doi.org/10.1111/ter.12404

Bachmann, O., Dungan, M. A., & Lipman, P. W. (2002). The Fish Canyon magma body, San Juan volcanic field, Colorado: Rejuvenation and eruption of an upper-crustal batholith. *Journal of Petrology*, *43*(8), 1469–1503. https://doi.org/10.1093/petrology/43.8.1469

Ballato, P., Uba, C. E., Landgraf, A., Strecker, M. R., Sudo, M., Stockli, D. F., et al. (2011). Arabia-Eurasia continental collision: Insights from late Tertiary foreland-basin evolution in the Alborz Mountains, northern Iran. *Geological Society of America Bulletin*, *123*(1–2), 106–131. https://doi.org/10.1130/B30091.1

Barber, D. E., Stockli, D. F., Horton, B. K., & Koshnaw, R. I. (2018). Cenozoic exhumation and Foreland Basin evolution of the Zagros Orogen during the Arabia-Eurasia collision, Western Iran. *Tectonics*, *37*(12), 4396–4420. https://doi.org/10.1029/2018TC005328

Bell, K., Castorina, F., Lavecchia, G., Rosatelli, G., & Stoppa, F. (2004). Is there a mantle plume below Italy? *Eos, Transactions American Geophysical Union*, *85*(50), 541–547. https://doi.org/10.1029/2004EO500002

Berberian, M., & King, G. C. P. (1981). Towards a paleogeography and tectonic evolution of Iran. *Canadian Journal of Earth Sciences*, *18*(2), 210–265. https://doi.org/10.1139/e81-019

Bonnet, G., Agard, P., Angiboust, S., Fournier, M., & Omrani, J. (2019). No large earthquakes in fully exposed subducted seamount. *Geology*, *47*(5), 407–410. https://doi.org/10.1130/G45564.1

Brunet, M.-F., Korotaev, M. V., Ershov, A. V., & Nikishin, A. M. (2003). The South Caspian Basin: A review of its evolution from subsidence modelling. *Sedimentary Geology*, *156*(1–4), 119–148. https://doi.org/10.1016/S0037-0738(02)00285-3

Burg, J.-P. (2018). Geology of the onshore Makran accretionary wedge: Synthesis and tectonic interpretation. *Earth-Science Reviews*, *185*, 1210–1231. https://doi.org/10.1016/j.earscirev.2018.09.011

Castillo, P. R. (2012). Adakite petrogenesis. *Lithos*, *134–135*(0), 304–316. https://doi.org/10.1016/j.lithos.2011.09.013

Castro, A., Aghazadeh, M., Badrzadeh, Z., & Chichorro, M. (2013). Late Eocene-Oligocene post-collisional monzonitic intrusions from the Alborz magmatic belt, NW Iran. An example of monzonite magma generation from a metasomatized mantle source. *Lithos*, *180*, 109–127. https://doi.org/10.1016/j.lithos.2013.08.003

Chapman, J. B., & Ducea, M. N. (2019). The role of arc migration in Cordilleran orogenic cyclicity. *Geology*, *47*(7), 627–631. https://doi.org/10.1130/G46117.1

Chapman, J. B., Ducea, M. N., Kapp, P., Gehrels, G. E., & DeCelles, P. G. (2017). Spatial and temporal radiogenic isotopic trends of magmatism in Cordilleran orogens. *Gondwana Research*, *48*, 189–204. https://doi.org/10.1016/j.gr.2017.04.019

Chauvel, C., & Blichert-Toft, J. (2001). A hafnium isotope and trace element perspective on melting of the depleted mantle. *Earth and Planetary Science Letters*, *190*(3), 137–151.

Chiu, H. Y., Chung, S. L., Zarrinkoub, M. H., Melkonyan, R., Pang, K. N., Lee, H. Y., et al. (2017). Zircon Hf isotopic constraints on magmatic and tectonic evolution in Iran: Implications for crustal growth in the Tethyan orogenic belt. *Journal of Asian Earth Sciences*, *145*, 652–669. https://doi.org/10.1016/j.jseaes.2017.06.011

Chiu, H. Y., Chung, S. L., Zarrinkoub, M. H., Mohammadi, S. S., Khatib, M. M., & Iizuka, Y. (2013). Zircon U-Pb age constraints from Iran on the magmatic evolution related to Neotethyan subduction and Zagros orogeny. *Lithos*, *162*, 70–87. https://doi.org/10.1016/j.lithos.2013.01.006

Churikova, T., Dorendorf, F., & Worner, G. (2001). Sources and fluids in the mantle wedge below Kamchatka, evidence from across-arc geochemical variation. *Journal of Petrology*, *42*(8), 1567–1593. https://doi.org/10.1093/petrology/42.8.1567

Davidson, J., Turner, S., Handley, H., Macpherson, C., & Dosseto, A. (2007). Amphibole "sponge" in arc crust? *Geology*, *35*(9), 787–790. https://doi.org/10.1130/G23637A.1

Davidson, J. P., Hora, J. M., Garrison, J. M., & Dungan, M. A. (2005). Crustal forensics in arc magmas. *Journal of Volcanology and Geothermal Research*, *140*(1–3), 157–170. https://doi.org/10.1016/j.jvolgeores.2004.07.019

Davidson, J. P., McMillan, N. J., Moorbath, S., Wörner, G., Harmon, R. S., & Lopez-Escobar, L. (1990). The Nevados de Payachata volcanic region (18 S/69 W, N. Chile) II. Evidence for widespread crustal involvement in Andean magmatism. *Contributions to Mineralogy and Petrology*, *105*(4), 412–432. https://doi.org/10.1007/BF00286829

DeCelles, P. G., Ducea, M. N., Kapp, P., & Zandt, G. (2009). Cyclicity in Cordilleran orogenic systems. *Nature Geoscience*, *2*(4), 251–257. https://doi.org/10.1038/ngeo469

Deevsalar, R., Shinjo, R., Ghaderi, M., Murata, M., Hoskin, P. W. O., Oshiro, S., et al. (2017). Mesozoic-Cenozoic mafic magmatism in Sanandaj-Sirjan Zone, Zagros Orogen (Western Iran): Geochemical and isotopic inferences from Middle Jurassic and Late Eocene gabbros. *Lithos*, *284*, 588–607. https://doi.org/10.1016/j.lithos.2017.05.009

Defant, M. J., & Drummond, M. S. (1990). Derivation of some modern arc magmas by melting of young subducted lithosphere. *Nature*, *347*(6294), 662–665. https://doi.org/10.1038/347662a0

Dercourt, J., Zonenshain, L. P., Ricou, L. E., Kazmin, V. G., Lepichon, X., Knipper, A. L., et al. (1986). Geological evolution of the Tethys Belt from the Atlantic to the Pamirs since the Lias. *Tectonophysics*, *123*(1–4), 241–315. https://doi.org/10.1016/0040-1951(86)90199-X

Dickinson, W. R., & Hatherton, T. (1967). Andesitic volcanism and seismicity around the Pacific. *Science*, *157*(3790), 801–803. https://doi.org/10.1126/science.157.3790.801

Ducea, M. N., & Barton, M. D. (2007). Igniting flare-up events in Cordilleran arcs. *Geology*, *35*(11), 1047–1050. https://doi.org/10.1130/G23898A.1

Ducea, M. N., Bergantz, G. W., Crowley, J. L., & Otamendi, J. (2017). Ultrafast magmatic buildup and diversification to produce continental crust during subduction. *Geology*, *45*(3), 235–238. https://doi.org/10.1130/G38726.1

Ducea, M. N., Paterson, S. R., & DeCelles, P. G. (2015a). High-volume magmatic events in subduction systems. *Elements*, *11*(2), 99–104. https://doi.org/10.2113/gselements.11.2.99

Ducea, M. N., Saleeby, J. B., & Bergantz, G. (2015b). The architecture, chemistry, and evolution of continental magmatic arcs. *Annual Review of Earth and Planetary Sciences*, *43*(1), 299–331. https://doi.org/10.1146/annurev-earth-060614-105049

Entezar-Saadat, V., Motavalli-Anbaran, S.-H., & Zeyen, H. (2017). Lithospheric structure of the eastern Iranian plateau from integrated geophysical modeling: A transect from Makran to the Turan platform. *Journal of Asian Earth Sciences*, *138*, 357–366. https://doi.org/10.1016/j.jseaes.2017.02.024

Ersoy, E. Y., & Palmer, M. R. (2013). Eocene-Quaternary magmatic activity in the Aegean: Implications for mantle metasomatism and magma genesis in an evolving orogeny. *Lithos*, *180*, 5–24. https://doi.org/10.1016/j.lithos.2013.06.007

Ferrari, L., Lopez-Martinez, M., Orozco-Esquivel, T., Bryan, S. E., Duque-Trujillo, J., Lonsdale, P., & Solari, L. (2013). Late Oligocene to Middle Miocene rifting and synextensional magmatism in the southwestern Sierra Madre Occidental, Mexico. *The beginning of the Gulf of California rift: Geosphere*, *9*(5), 1161–1200.

Ghalamghash, J., Nedelec, A., Bellon, H., Abedini, M. V., & Bouchez, J. L. (2009). The Urumieh plutonic complex (NW Iran): A record of the geodynamic evolution of the Sanandaj-Sirjan zone during Cretaceous times—Part I: Petrogenesis and K/Ar dating. *Journal of Asian Earth Sciences*, *35*(5), 401–415. https://doi.org/10.1016/j.jseaes.2009.02.002

Ghasemi, A., & Talbot, C. J. (2006). A new tectonic scenario for the Sanandaj-Sirjan Zone (Iran). *Journal of Asian Earth Sciences*, *26*(6), 683–693. https://doi.org/10.1016/j.jseaes.2005.01.003

Ghorbani, M. R., Graham, I. T., & Ghaderi, M. (2014). Oligocene-Miocene geodynamic evolution of the central part of Urumieh-Dokhtar Arc of Iran. *International Geology Review*, *56*(8), 1039–1050. https://doi.org/10.1080/00206814.2014.919615

Golonka, J. (2004). Plate tectonic evolution of the southern margin of Eurasia in the Mesozoic and Cenozoic. *Tectonophysics*, *381*(1–4), 235–273. https://doi.org/10.1016/j.tecto.2002.06.004

Haq, B. U., & Al-Qahtani, A. M. (2005). Phanerozoic cycles of sea-level change on the Arabian Platform. *Geoarabia*, *10*(2), 127–160.

Hart, S., & Hauri, E. (1992). Mantle plumes and entrainment: isotopic evidence. *Science*, *256*(5056), 517–520. https://doi.org/10.1126/science.256.5056.517

Hassanzadeh, J., Stockli, D. F., Horton, B. K., Axen, G. J., Stockli, L. D., Grove, M., et al. (2008). U-Pb zircon geochronology of late Neoproterozoic-Early Cambrian granitoids in Iran: Implications for paleogeography, magmatism, and exhumation history of Iranian basement. *Tectonophysics*, *451*(1–4), 71–96. https://doi.org/10.1016/j.tecto.2007.11.062

Hawkesworth, C. J., & Kemp, A. I. S. (2006). Using hafnium and oxygen isotopes in zircons to unravel the record of crustal evolution. *Chemical Geology*, *226*(3–4), 144–162. https://doi.org/10.1016/j.chemgeo.2005.09.018

Heydolph, K., Hoernle, K., Hauff, F., van den Bogaard, P., Portnyagin, M., Bindeman, I., & Garbe-Schonberg, D. (2012a). Along and across arc geochemical variations in NW Central America: Evidence for involvement of lithospheric pyroxenite. *Geochimica et Cosmochimica Acta*, *84*, 459–491. https://doi.org/10.1016/j.gca.2012.01.035

Heydolph, K., Hoernle, K., Hauff, F., van den Bogaard, P., Portnyagin, M., Bindeman, I., & Garbe-Schönberg, D. (2012b). Along and across arc geochemical variations in NW Central America: Evidence for involvement of lithospheric pyroxenite. *Geochimica et Cosmochimica Acta*, *84*, 459–491. https://doi.org/10.1016/j.gca.2012.01.035

Hochstaedter, A., Gill, J., Peters, R., Broughton, P., Holden, P., & Taylor, B. (2001). Across-arc geochemical trends in the Izu-Bonin arc: Contributions from the subducting slab. *Geochemistry, Geophysics, Geosystems*, *2*(7), n/a–n/a. https://doi.org/10.1029/2000GC000105

Honarmand, M., Omran, N. R., Corfu, F., Emami, M. H., & Nabatian, G. (2013). Geochronology and magmatic history of a calc-alkaline plutonic complex in the Urumieh-Dokhtar Magmatic Belt, Central Iran: Zircon ages as evidence for two major plutonic episodes. *Neues Jahrbuch Fur Mineralogie-Abhandlungen*, *190*(1), 67–77. https://doi.org/10.1127/0077-7757/2013/0230

Hosseini, M. R., Hassanzadeh, J., Alirezaei, S., Sun, W. D., & Li, C. Y. (2017). Age revision of the Neotethyan arc migration into the southeast Urumieh-Dokhtar belt of Iran: Geochemistry and U-Pb zircon geochronology. *Lithos*, *284*, 296–309. https://doi.org/10.1016/j.lithos.2017.03.012

Huang, F., & Lundstrom, C. C. (2007). 231Pa excesses in arc volcanic rocks: Constraint on melting rates at convergent margins. *Geology*, *35*(11), 1007. https://doi.org/10.1130/G23822A.1

Hunziker, D., Burg, J. P., Bouilhol, P., & von Quadt, A. (2015). Jurassic rifting at the Eurasian Tethys margin: Geochemical and geochronological constraints from granitoids of North Makran, southeastern Iran. *Tectonics*, *34*(3), 571–593. https://doi.org/10.1002/2014TC003768

Iannelli, S. B., Fennell, L. M., Litvak, V. D., Lucía, F. P., Alfonso, E., & Andrés, F. (2018). Geochemical and tectonic evolution of Late Cretaceous to early Paleocene magmatism along the Southern Central Andes (35-36° S). *Journal of South American Earth Sciences*, *87*, 139–156. https://doi.org/10.1016/j.jsames.2017.12.008

Ishizuka, O., Taylor, R. N., Milton, J. A., & Nesbitt, R. W. (2003). Fluid-mantle interaction in an intra-oceanic arc: Constraints from high-precision Pb isotopes. *Earth and Planetary Science Letters*, *211*(3–4), 221–236. https://doi.org/10.1016/S0012-821X(03)00201-2

Jacques, G., Hoernle, K., Gill, J., Hauff, F., Wehrmann, H., Garbe-Schönberg, D., et al. (2013). Across-arc geochemical variations in the Southern Volcanic Zone, Chile (34.5–38.0 S): Constraints on mantle wedge and slab input compositions. *Geochimica et Cosmochimica Acta*, *123*, 218–243. https://doi.org/10.1016/j.gca.2013.05.016

Jacques, G., Hoernle, K., Gill, J., Wehrmann, H., Bindeman, I., & Lara, L. E. (2014). Geochemical variations in the Central Southern Volcanic Zone, Chile (38–43 S): The role of fluids in generating arc magmas. *Chemical Geology*, *371*, 27–45. https://doi.org/10.1016/j.chemgeo.2014.01.015

Jakes, P., & White, A. (1969). Structure of the Melanesian arcs and correlation with distribution of magma types. *Tectonophysics*, *8*(3), 223–236. https://doi.org/10.1016/0040-1951(69)90099-7

Kay, S. M., & Coira, B. L. (2009). Shallowing and steepening subduction zones, continental lithospheric loss, magmatism, and crustal flow under the Central Andean Altiplano-Puna Plateau: Backbone of the Americas. *Shallow Subduction, Plateau Uplift, and Ridge and Terrane Collision*, *204*, 229–259. https://doi.org/10.1130/2009.1204(11)

Kazemi, Z., Ghasemi, H., Tilhac, R., Griffin, W., Moghadam, H. S., O'Reilly, S., & Mousivand, F. (2019). Late Cretaceous subduction-related magmatism on the southern edge of Sabzevar basin, NE Iran. *Journal of the Geological Society*, *176*(3), 530–552. https://doi.org/10.1144/jgs2018-076

Kazmin, V. G., Sbortshikov, I. M., Ricou, L. E., Zonenshain, L. P., Boulin, J., & Knipper, A. L. (1986). Volcanic belts as markers of the Mesozoic-Cenozoic active margin of Eurasia. *Tectonophysics*, *123*(1–4), 123–152. https://doi.org/10.1016/0040-1951(86)90195-2

Kheirkhah, M., Neill, I., & Allen, M. B. (2015). Petrogenesis of OIB-like basaltic volcanic rocks in a continental collision zone: Late Cenozoic magmatism of Eastern Iran. *Journal of Asian Earth Sciences*, *106*, 19–33. https://doi.org/10.1016/j.jseaes.2015.02.027

Kimura, J. I., Kent, A. J. R., Rowe, M. C., Katakuse, M., Nakano, F., Hacker, B. R., et al. (2010). Origin of cross-chain geochemical variation in Quaternary lavas from the northern Izu arc: Using a quantitative mass balance approach to identify mantle sources and mantle wedge processes. *Geochemistry, Geophysics, Geosystems*, *11*, 227–249. https://doi.org/10.1016/j.lithos.2017.12.003

Kimura, J.-I., Sakuyama, T., Miyazaki, T., Vaglarov, B. S., Fukao, Y., & Stern, R. J. (2018). Plume-stagnant slab-lithosphere interactions: Origin of the late Cenozoic intra-plate basalts on the East Eurasia margin. *Lithos*, *300*, 227–249. https://doi.org/10.1016/j.lithos.2017.12.003

Kodaira, S., Noguchi, N., Takahashi, N., Ishizuka, O., & Kaneda, Y. (2010). Evolution from fore-arc oceanic crust to island arc crust: A seismic study along the Izu-Bonin fore arc. *Journal of Geophysical Research*, *115*(B9), B09102. https://doi.org/10.1029/2009JB006968

Koshnaw, R. I., Horton, B. K., Stockli, D. F., Barber, D. E., Tamar-Agha, M. Y., & Kendall, J. J. (2017). Neogene shortening and exhumation of the Zagros fold-thrust belt and foreland basin in the Kurdistan region of northern Iraq. *Tectonophysics*, *694*, 332–355. https://doi.org/10.1016/j.tecto.2016.11.016

Koshnaw, R. I., Stockli, D. F., & Schlunegger, F. (2019). Timing of the Arabia-Eurasia continental collision—Evidence from detrital zircon U-Pb geochronology of the Red Bed Series strata of the northwest Zagros hinterland, Kurdistan region of Iraq Reply. *Geology*, *47*(8), E472–E472. https://doi.org/10.1130/G46438Y.1

Kuno, H. (1966). Lateral variation of basalt magma type across continental margins and island arcs. *Bulletin Volcanologique*, *29*(1), 195–222. https://doi.org/10.1007/BF02597153

Kuritani, T., & Nakagawa, M. (2016). Origin of ultra rear-arc magmatism at Rishiri Volcano, Kuril Arc. *Geochemistry, Geophysics, Geosystems*, *17*(10), 4032–4050. https://doi.org/10.1002/2016GC006594

Kuritani, T., Yokoyama, T., & Nakamura, E. (2008). Generation of rear-arc magmas induced by influx of slab-derived supercritical liquids: Implications from alkali basalt lavas from Rishiri volcano, Kurile arc. *Journal of Petrology*, *49*(7), 1319–1342. https://doi.org/10.1093/petrology/egn027

Lake, E. T., & Farmer, G. L. (2015). Oligo-Miocene mafic intrusions of the San Juan volcanic field, southwestern Colorado, and their relationship to voluminous, caldera-forming magmas. *Geochimica et Cosmochimica Acta*, *157*, 86–108. https://doi.org/10.1016/j.gca.2015.02.020

Le Maitre, R. W., Streckeisen, A., Zanettin, B., Le Bas, M. J., Bonin, B., and Bateman, P. C., 2002, Cambridge University Press, igneous rocks: A classification and glossary of terms: Recommendations of the International Union of Geological Sciences Subcommission on the Systematics of Igneous Rocks.

Lebas, M. J., Lemaitre, R. W., Streckeisen, A., & Zanettin, B. (1986). A chemical classification of volcanic-rocks based on the total alkali silica diagram. *Journal of Petrology*, *27*(3), 745–750. https://doi.org/10.1093/petrology/27.3.745

Lechmann, A., Burg, J.-P., Ulmer, P., Mohammadi, A., Guillong, M., & Faridi, M. (2018). From Jurassic rifting to Cretaceous subduction in NW Iranian Azerbaijan: Geochronological and geochemical signals from granitoids. *Contributions to Mineralogy and Petrology*, *173*(12), 102. https://doi.org/10.1007/s00410-018-1532-8

Linnemann, U., Ouzegane, K., Drareni, A., Hofmann, M., Becker, S., Gartner, A., & Sagawe, A. (2011). Sands of West Gondwana: An archive of secular magmatism and plate interactions—A case study from the Cambro-Ordovician section of the Tassili Ouan Ahaggar (Algerian Sahara) using U-Pb-LA-ICP-MS detrital zircon ages. *Lithos*, *123*(1–4), 188–203. https://doi.org/10.1016/j.lithos.2011.01.010

Malekpour-Alamdari, A., Axen, G., Heizler, M., & Hassanzadeh, J. (2017). Large-magnitude continental extension in the northeastern Iranian Plateau: Insight from K-feldspar 40Ar/39Ar thermochronology from the Shotor Kuh–Biarjmand metamorphic core complex. *Geosphere*, *13*(4), 1207–1233. https://doi.org/10.1130/ges01423.1

McQuarrie, N., & van Hinsbergen, D. J. J. (2013). Retrodeforming the Arabia-Eurasia collision zone: Age of collision versus magnitude of continental subduction. *Geology*, *41*(3), 315–318. https://doi.org/10.1130/G33591.1

Moghadam, H. S., Brocker, M., Griffin, W. L., Li, X. H., Chen, R. X., & O'Reilly, S. Y. (2017). Subduction, high-P metamorphism, and collision fingerprints in South Iran: Constraints from zircon U-Pb and mica Rb-Sr geochronology. *Geochemistry, Geophysics, Geosystems*, *18*(1), 306–332. https://doi.org/10.1002/2016GC006585

Moghadam, H. S., Corfu, F., Chiaradia, M., Stern, R. J., & Ghorbani, G. (2014). Sabzevar Ophiolite, NE Iran: Progress from embryonic oceanic lithosphere into magmatic arc constrained by new isotopic and geochemical data. *Lithos*, *210–211*, 224–241. https://doi.org/10.1016/j.lithos.2014.10.004

Moghadam, H. S., Corfu, F., & Stern, R. J. (2013). U-Pb zircon ages of Late Cretaceous Nain-Dehshir ophiolites, central Iran. *Journal of the Geological Society*, *170*(1), 175–184. https://doi.org/10.1144/jgs2012-066

Moghadam, H. S., Griffin, W. L., Kirchenbaur, M., Garbe-Schonberg, D., Khedr, M. Z., Kimura, J. I., et al. (2018). Roll-back, extension and mantle upwelling triggered Eocene potassic magmatism in NW Iran. *Journal of Petrology*, *59*(7), 1417–1465. https://doi.org/10.1093/petrology/egy067

Moghadam, H. S., Griffin, W. L., Li, X. H., Santos, J. F., Karsli, O., Stern, R. J., et al. (2017). Crustal evolution of NW Iran: Cadomian arcs, archean fragments and the Cenozoic magmatic flare-up. *Journal of Petrology*, *58*(11), 2143–2190. https://doi.org/10.1093/petrology/egy005

Moghadam, H. S., Khademi, M., Hu, Z. C., Stern, R. J., Santos, J. F., & Wu, Y. B. (2015). Cadomian (Ediacaran-Cambrian) arc magmatism in the ChahJam-Biarjmand metamorphic complex (Iran): Magmatism along the northern active margin of Gondwana. *Gondwana Research*, *27*(1), 439–452. https://doi.org/10.1016/j.gr.2013.10.014

Moghadam, H. S., Li, Q. L., Griffin, W. L., Stern, R. J., Ishizuka, O., Henry, H., et al. (2020). Repeated magmatic buildup and deep “ hot zones” in continental evolution: The Cadomian crust of Iran. *Earth and Planetary Science Letters*, *531*, 115989.

Moghadam, H. S., Li, X.-H., Griffin, W. L., Stern, R. J., Thomsen, T. B., Meinhold, G., et al. (2017). Early Paleozoic tectonic reconstruction of Iran: Tales from detrital zircon geochronology. *Lithos*, *268*, 87–101. https://doi.org/10.1016/j.lithos.2016.09.008

Moghadam, H. S., Li, X. H., Ling, X. X., Santos, J. F., Stern, R. J., Li, Q. L., & Ghorbani, G. (2015). Eocene Kashmar granitoids (NE Iran): Petrogenetic constraints from U-Pb zircon geochronology and isotope geochemistry. *Lithos*, *216*, 118–135. https://doi.org/10.1016/j.lithos.2014.12.012

Moghadam, H. S., Li, X. H., Stern, R. J., Ghorbani, G., & Bakhshizad, F. (2016). Zircon U-Pb ages and Hf-O isotopic composition of migmatites from the Zanjan-Takab complex, NW Iran: Constraints on partial melting of metasediments. *Lithos*, *240*, 34–48. https://doi.org/10.1016/j.lithos.2015.11.004

Moghadam, H. S., Li, X. H., Santos, J. F., Stern, R. J., Griffin, W. L., Ghorbani, G., & Sarebani, N. (2017). Neoproterozoic magmatic flare-up along the N. margin of Gondwana: The Taknar complex, NE Iran. *Earth and Planetary Science Letters*, *474*, 83–96. https://doi.org/10.1016/j.epsl.2017.06.028

Moghadam, H. S., Rossetti, F., Lucci, F., Chiaradia, M., Gerdes, A., Martinez, M. L., et al. (2016). The calc-alkaline and adakitic volcanism of the Sabzevar structural zone (NE Iran): Implications for the Eocene magmatic flare-up in Central Iran. *Lithos*, *248*, 517–535. https://doi.org/10.1016/j.lithos.2016.01.019

Moghadam, H. S., & Stern, R. J. (2011). Geodynamic evolution of Upper Cretaceous Zagros ophiolites: Formation of oceanic lithosphere above a nascent subduction zone. *Geological Magazine*, *148*(5–6), 762–801. https://doi.org/10.1017/S0016756811000410

Moghadam, H. S., & Stern, R. J. (2015). Ophiolites of Iran: Keys to understanding the tectonic evolution of SW Asia: (II) Mesozoic ophiolites. *Journal of Asian Earth Sciences*, *100*, 31–59. https://doi.org/10.1016/j.jseaes.2014.12.016

Moghadam, H. S., Stern, R. J., Griffin, W. L., Khedr, M. Z., Kirchenbaur, M., Ottley, C. J., et al. (2019). Subduction initiation and back-arc opening north of Neo-Tethys: Evidence from the Late Cretaceous Torbat-e-Heydarieh ophiolite of NE Iran: Geological Society of America Bulletin, v. 131.

Molinaro, M., Zeyen, H., & Laurencin, X. (2005). Lithospheric structure beneath the south-eastern Zagros Mountains, Iran: Recent slab break-off? *Terra Nova*, *17*(1), 1–6. https://doi.org/10.1111/j.1365-3121.2004.00575.x

Monsef, I., Monsef, R., Mata, J., Zhang, Z., Pirouz, M., Rezaeian, M., et al. (2018). Evidence for an early-MORB to fore-arc evolution within the Zagros suture zone: Constraints from zircon U-Pb geochronology and geochemistry of the Neyriz ophiolite (South Iran). *Gondwana Research*, *62*, 287–305. https://doi.org/10.1016/j.gr.2018.03.002

Moritz, R., Ghazban, F., & Singer, B. S. (2006). Eocene gold ore formation at Muteh, Sanandaj-Sirjan tectonic zone, western Iran: A result of late-stage extension and exhumation of metamorphic basement rocks within the Zagros orogen. *Economic Geology*, *101*(8), 1497–1524. https://doi.org/10.2113/gsecongeo.101.8.1497

Mottaghi, A. A., Rezapour, M., & Korn, M. (2013). Ambient noise surface wave tomography of the Iranian Plateau. *Geophysical Journal International*, *193*(1), 452–462. https://doi.org/10.1093/gji/ggs134

Murphy, J. B., Pisarevsky, S. A., Nance, R. D., & Keppie, J. D. (2004). Neoproterozoic—Early Paleozoic evolution of peri-Gondwanan terranes: Implications for Laurentia-Gondwana connections. *International Journal of Earth Sciences*, *93*(5), 659–682. https://doi.org/10.1007/s00531-004-0412-9

Nance, R. D., Gutierrez-Alonso, G., Keppie, J. D., Linnemann, U., Murphy, J. B., Quesada, C., et al. (2010). Evolution of the Rheic Ocean. *Gondwana Research*, *17*(2–3), 194–222. https://doi.org/10.1016/j.gr.2009.08.001

Neill, I., Meliksetian, K., Allen, M. B., Navasardyan, G., & Kuiper, K. (2015). Petrogenesis of mafic collision zone magmatism: The Armenian sector of the Turkish-Iranian Plateau. *Chemical Geology*, *403*, 24–41. https://doi.org/10.1016/j.chemgeo.2015.03.013

Neubauer, F. (2002). Evolution of late Neoproterozoic to early Paleozoic tectonic elements in Central and Southeast European Alpine mountain belts: Review and synthesis. *Tectonophysics*, *352*(1–2), 87–103. https://doi.org/10.1016/S0040-1951(02)00190-7

Nouri, F., Azizi, H., Golonka, J., Asahara, Y., Orihashi, Y., Yamamoto, K., et al. (2016). Age and petrogenesis of Na-rich felsic rocks in western Iran: Evidence for closure of the southern branch of the Neo-Tethys in the Late Cretaceous. *Tectonophysics*, *671*, 151–172. https://doi.org/10.1016/j.tecto.2015.12.014

Nowell, G., Kempton, P., Noble, S., Fitton, J., Saunders, A., Mahoney, J., & Taylor, R. (1998). High precision Hf isotope measurements of MORB and OIB by thermal ionisation mass spectrometry: Insights into the depleted mantle. *Chemical Geology*, *149*(3-4), 211–233. https://doi.org/10.1016/S0009-2541(98)00036-9

Pang, K. N., Chung, S. L., Zarrinkoub, M. H., Khatib, M. M., Mohammadi, S. S., Chiu, H. Y., et al. (2013). Eocene-Oligocene post-collisional magmatism in the Lut-Sistan region, eastern Iran: Magma genesis and tectonic implications. *Lithos*, *180*, 234–251. https://doi.org/10.1016/j.lithos.2013.05.009

Pang, K.-N., Chung, S.-L., Zarrinkoub, M. H., Li, X.-H., Lee, H.-Y., Lin, T.-H., & Chiu, H.-Y. (2016). New age and geochemical constraints on the origin of Quaternary adakite-like lavas in the Arabia–Eurasia collision zone. *Lithos*, *264*, 348–359. https://doi.org/10.1016/j.lithos.2016.08.042

Pang, K. N., Chung, S. L., Zarrinkoub, M. H., Mohammadi, S. S., Yang, H. M., Chu, C. H., et al. (2012). Age, geochemical characteristics and petrogenesis of Late Cenozoic intraplate alkali basalts in the Lut-Sistan region, eastern Iran. *Chemical Geology*, *306*, 40–53. https://doi.org/10.1016/j.chemgeo.2012.02.020

Pang, K.-N., Chung, S.-L., Zarrinkoub, M. H., Wang, F., Kamenetsky, V. S., & Lee, H.-Y. (2015). Quaternary high-Mg ultrapotassic rocks from the Qal'eh Hasan Ali maars, southeastern Iran: Petrogenesis and geodynamic implications. *Contributions to Mineralogy and Petrology*, *170*(3), 27. https://doi.org/10.1007/s00410-015-1183-y

Paterson, S. R., & Ducea, M. N. (2015). Arc magmatic tempos: Gathering the evidence. *Elements*, *11*(2), 91–98. https://doi.org/10.2113/gselements.11.2.91

Paterson, S. R., Okaya, D., Memeti, V., Economos, R., & Miller, R. B. (2011). Magma addition and flux calculations of incrementally constructed magma chambers in continental margin arcs: Combined field, geochronologic, and thermal modeling studies. *Geosphere*, *7*(6), 1439–1468. https://doi.org/10.1130/GES00696.1

Paz, L. F., Bechis, F., Litvak, V. D., Echaurren, A., Encinas, A., González, J., et al. (2019). Constraints on trenchward arc migration and back-arc magmatism in the North Patagonian Andes in the context of Nazca plate rollback. *Tectonics*, *38*(11), 3794–3817. https://doi.org/10.1029/2019tc005580

Pearce, J., Kempton, P., Nowell, G., & Noble, S. (1999). Hf-Nd element and isotope perspective on the nature and provenance of mantle and subduction components in Western Pacific arc-basin systems. *Journal of Petrology*, *40*(11), 1579–1611. https://doi.org/10.1093/petroj/40.11.1579

Pereira, M. F., Chichorro, M., Linnemann, U., Eguiluz, L., & Silva, J. B. (2006). Inherited arc signature in Ediacaran and Early Cambrian basins of the Ossa-Morena Zone (Iberian Massif, Portugal): Paleogeographic link with European and North African Cadomian correlatives. *Precambrian Research*, *144*(3–4), 297–315. https://doi.org/10.1016/j.precamres.2005.11.011

Ramezani, J., & Tucker, R. D. (2003). The Saghand region, Central Iran: U-Pb geochronology, petrogenesis and implications for Gondwana Tectonics. *American Journal of Science*, *303*(7), 622–665. https://doi.org/10.2475/ajs.303.7.622

Rivandi, B., Vahidinia, M., Nadjafi, M., Mahboubi, A., & Sadeghi, A. (2013). Sequence and biostratigraphy of lower Cenozoic succession in the Kopet-Dagh Basin, NE of Iran. *Open Journal of Geology*, *03*(03), 240–249. https://doi.org/10.4236/ojg.2013.33028

Seebeck, H., Nicol, A., Giba, M., Pettinga, J., & Walsh, J. (2014). Geometry of the subducting Pacific plate since 20 Ma, Hikurangi margin, New Zealand. *Journal of the Geological Society*, *171*(1), 131–143. https://doi.org/10.1144/jgs2012-145

Sepidbar, F., Mirnejad, H., Ma, C., & Moghadam, H. S. (2018). Identification of Eocene-Oligocene magmatic pulses associated with flare-up in east Iran: Timing and sources. *Gondwana Research*, *57*, 141–156. https://doi.org/10.1016/j.gr.2018.01.008

Sepidbar, F., Shafaii Moghadam, H., Zhang, L., Li, J.-W., Ma, J., Stern, R. J., & Lin, C. (2019). Across-arc geochemical variations in the Paleogene magmatic belt of Iran. *Lithos*, *344-345*, 280–296. https://doi.org/10.1016/j.lithos.2019.06.022

Shakerardakani, F., Li, X.-H., Ling, X.-X., Li, J., Tang, G.-Q., Liu, Y., & Monfaredi, B. (2019). Evidence for Archean crust in Iran provided by ca 2.7 Ga zircon xenocrysts within amphibolites from the Sanandaj–Sirjan zone, Zagros orogen. *Precambrian Research*, *332*, 105390. https://doi.org/10.1016/j.precamres.2019.105390

Shellnutt, J. G., Lee, T. Y., Brookfield, M. E., & Chung, S. L. (2014). Correlation between magmatism of the Ladakh Batholith and plate convergence rates during the India-Eurasia collision. *Gondwana Research*, *26*(3–4), 1051–1059. https://doi.org/10.1016/j.gr.2013.09.006

Shomali, Z. H., Keshvari, F., Hassanzadeh, J., & Mirzaei, N. (2011). Lithospheric structure beneath the Zagros collision zone resolved by non-linear teleseismic tomography. *Geophysical Journal International*, *187*(1), 394–406. https://doi.org/10.1111/j.1365-246X.2011.05150.x

Skipton, D. R., Dunning, G. R., & Sparkes, G. W. (2013). Late Neoproterozoic arc-related magmatism in the Horse Cove Complex, eastern Avalon Zone, Newfoundland. *Canadian Journal of Earth Sciences*, *50*(4), 462–482. https://doi.org/10.1139/cjes-2012-0090

Stampfli, G., Marcoux, J., & Baud, A. (1991). Tethyan margins in space and time. *Palaeogeography Palaeoclimatology Palaeoecology*, *87*(1–4), 373–409. https://doi.org/10.1016/0031-0182(91)90142-E

Stern, R. J. (2004). Subduction initiation: Spontaneous and induced. *Earth and Planetary Science Letters*, *226*(3–4), 275–292. https://doi.org/10.1016/S0012-821X(04)00498-4

Stern, R. J., & Gerya, T. (2018). Subduction initiation in nature and models: A review. *Tectonophysics*, *746*, 173–198.

Stern, R. J., & Johnson, P. (2010). Continental lithosphere of the Arabian Plate: A geologic, petrologic, and geophysical synthesis. *Earth-Science Reviews*, *101*(1–2), 29–67. https://doi.org/10.1016/j.earscirev.2010.01.002

Stockli, D., 2004, Structural and geochronological evidence for Oligo–Miocene intra–arc low angle detachment faulting in the Takab–Zanjan area, NW Iran, abstract with programs. Geological Society of America, p. 319.

Streckeisen, A. (1979a). Classification and nomenclature of volcanic-rocks, lamprophyres, carbonatites, and melilitic rocks—Recommendations and suggestions of the IUGS sub-commission on the systematics of igneous rocks. *Geology*, *7*(7), 331–335. https://doi.org/10.1130/0091-7613(1979)7<331:CANOVR>2.0.CO;2

Streckeisen, A. (1979b). Classification of volcanic-rocks, lamprophyres, carbonatites, and melilitic rocks—Recommendations and suggestions of the IUGS subcommission on the systematics of igneous rocks—Reply. *Geology*, *7*(12), 562–562. https://doi.org/10.1130/0091-7613(1979)7<562b:CAROCO>2.0.CO;2

Sun, S.-S., & McDonough, W.-S. (1989). Chemical and isotopic systematics of oceanic basalts: Implications for mantle composition and processes. *Geological Society, London, Special Publications*, *42*(1), 313–345. https://doi.org/10.1144/GSL.SP.1989.042.01.19

Tadayon, M., Rossetti, F., Zattin, M., Calzolari, G., Nozaem, R., Salvini, F., et al., 2018, The long-term evolution of the Doruneh Fault region (Central Iran): A key to understanding the spatio-temporal tectonic evolution in the hinterland of the Zagros convergence zone: Geological Journal, p. 1–26.

Tamura, Y., Kodaira, S., Ishizuka, O., Kawabata, H., Suzuki, T., Chang, Q., & Tatsumi, Y. (2007). Silicic magmas in the Izu-Bonin oceanic arc and implications for crustal evolution. *Geochimica et Cosmochimica Acta*, *71*(15), A998–A998.

Tatsumi, Y., & Kogiso, T. (2003). The subduction factory: Its role in the evolution of the Earth's crust and mantle. *Geological society*, London, Special Publications, *219*(1), 55–80.

Todd, E., Gill, J. B., Wysoczanski, R. J., Hergt, J., Wright, I. C., Leybourne, M. I., & Mortimer, N. (2011). Hf isotopic evidence for small-scale heterogeneity in the mode of mantle wedge enrichment: Southern Havre Trough and South Fiji Basin back arcs. *Geochemistry, Geophysics, Geosystems*, *12*(9), n/a–n/a. https://doi.org/10.1029/2011gc003683

van Hinsbergen, D. J., Maffione, M., Koornneef, L. M., & Guilmette, C. (2019). Kinematic and paleomagnetic restoration of the Semail ophiolite (Oman) reveals subduction initiation along an ancient Neotethyan fracture zone. *Earth and Planetary Science Letters*, *518*, 183–196. https://doi.org/10.1016/j.epsl.2019.04.038

Verdel, C., Wernicke, B. P., Hassanzadeh, J., & Guest, B. (2011a). A Paleogene extensional arc flare-up in Iran. *Tectonics*, *30*(3), n/a. https://doi.org/10.1029/2010TC002809

Verdel, C., Wernicke, B. P., Ramezani, J., Hassanzadeh, J., Renne, P. R., & Spell, T. L. (2007). Geology and thermochronology of Tertiary Cordilleran-style metamorphic core complexes in the Saghand region of central Iran. *Geological Society of America Bulletin*, *119*(7–8), 961–977. https://doi.org/10.1130/B26102.1

Verges, J., Saura, E., Casciello, E., Fernandez, M., Villasenor, A., Jimenez-Munt, I., & Garcia-Castellanos, D. (2011). Crustal-scale cross-sections across the NW Zagros belt: Implications for the Arabian margin reconstruction. *Geological Magazine*, *148*(5–6), 739–761. https://doi.org/10.1017/S0016756811000331

Vervoort, J. D., & Blichert-Toft, J. (1999). Evolution of the depleted mantle: Hf isotope evidence from juvenile rocks through time. *Geochimica et Cosmochimica Acta*, *63*(3-4), 533–556. https://doi.org/10.1016/S0016-7037(98)00274-9

Vincent, S. J., Allen, M. B., Ismail-Zadeh, A. D., Flecker, R., Foland, K. A., & Simmons, M. D. (2005). Insights from the Talysh of Azerbaijan into the Paleogene evolution of the South Caspian region. *Geological Society of America Bulletin*, *117*(11), 1513–1533. https://doi.org/10.1130/B25690.1

von Raumer, J. F., Stampfli, G. A., & Bussy, F. (2003). Gondwana-derived microcontinents—The constituents of the Variscan and Alpine collisional orogens. *Tectonophysics*, *365*(1–4), 7–22. https://doi.org/10.1016/S0040-1951(03)00015-5

von Raumer, J. F., Stampfli, G. M., Borel, G., & Bussy, F. (2002). Organization of pre-Variscan basement areas at the north-Gondwanan margin. *International Journal of Earth Sciences*, *91*(1), 35–52. https://doi.org/10.1007/s005310100200

Woodhead, J., Hergt, J., Davidson, J., & Eggins, S. (2001). Hafnium isotope evidence for "conservative" element mobility during subduction zone processes. *Earth and Planetary Science Letters*, *192*(3), 331–346. https://doi.org/10.1016/S0012-821X(01)00453-8

Zanchi, A., Malaspina, N., Zanchetta, S., Berra, F., Benciolini, L., Bergomi, M., et al. (2015). The Cimmerian accretionary wedge of Anarak, Central Iran. *Journal of Asian Earth Sciences*, *102*, 45–72. https://doi.org/10.1016/j.jseaes.2014.08.030

Zhang, X., Chung, S.-L., Lai, Y.-M., Ghani, A. A., Murtadha, S., Lee, H.-Y., & Hsu, C.-C. (2019). A 6000-km-long Neo-Tethyan arc system with coherent magmatic flare-ups and lulls in South Asia. *Geology*, *47*(6), 573–576. https://doi.org/10.1130/G46172.1

Zindler, A., & Hart, S. (1986). Chemical geodynamics. *Annual Review of Earth and Planetary Sciences*, *14*(1), 493–571. https://doi.org/10.1146/annurev.ea.14.050186.002425

Zulauf, G., Dorr, W., Fiala, J., & Vejnar, Z. (1997). Late Cadomian crustal tilting and Cambrian transtension in the Tepla-Barrandian unit (Bohemian Massif, Central European Variscides). *Geologische Rundschau*, *86*(3), 571–584. https://doi.org/10.1007/s005310050164

References From the Supporting Information

Corfu, F. (2004). U-Pb age, setting and tectonic significance of the anorthosite-mangerite-charnockite-granite suite, Lofoten-Vesteralen, Norway. *Journal of Petrology*, *45*(9), 1799–1819. https://doi.org/10.1093/petrology/egh034

Corfu, F., Hanchar, J. M., Hoskin, P. W. O., & Kinny, P. (2003). Atlas of zircon textures. *Zircon*, *53*, 469–500. https://doi.org/10.1515/9781501509322-019

Depaolo, D. J. (1981). Trace-element and isotopic effects of combined wallrock assimilation and fractional crystallization. *Earth and Planetary Science Letters*, *53*(2), 189–202. https://doi.org/10.1016/0012-821X(81)90153-9

Griffin, W. L., Wang, X., Jackson, S. E., Pearson, N. J., O'Reilly, S. Y., Xu, X. S., & Zhou, X. M. (2002). Zircon chemistry and magma mixing, SE China: In-situ analysis of Hf isotopes, Tonglu and Pingtan igneous complexes. *Lithos*, *61*(3–4), 237–269. https://doi.org/10.1016/S0024-4937(02)00082-8

Li, X. H., Li, W. X., Li, Q. L., Wang, X. C., Liu, Y., & Yang, Y. H. (2010b). Petrogenesis and tectonic significance of the similar to 850 Ma Gangbian alkaline complex in South China: Evidence from in situ zircon U-Pb dating, Hf-O isotopes and whole-rock geochemistry. *Lithos*, *114*(1–2), 1–15. https://doi.org/10.1016/j.lithos.2009.07.011

Li, X. H., Long, W. G., Li, Q. L., Liu, Y., Zheng, Y. F., Yang, Y. H., et al. (2010a). Penglai zircon megacrysts: A potential new working reference material for microbeam determination of Hf-O isotopes and U-Pb age. *Geostandards and Geoanalytical Research*, *34*(2), 117–134. https://doi.org/10.1111/j.1751-908X.2010.00036.x

Li, X. H., Tang, G. Q., Gong, B., Yang, Y. H., Hou, K. J., Hu, Z. C., et al. (2013). Qinghu zircon: A working reference for microbeam analysis of U-Pb age and Hf and O isotopes. *Chinese Science Bulletin*, *58*(36), 4647–4654. https://doi.org/10.1007/s11434-013-5932-x

Ludwig, K. R. (2003). User's Manual for Isoplot 3.00: A Geochronological Toolkit for Microsoft Excel.

Nasdala, L., Hofmeister, W. G., Norberg, N., Mattinson, J. M., Corfu, F., Dorr, W., et al. (2008). Zircon M257—A homogeneous natural reference material for the ion microprobe U-Pb analysis of zircon. *Geostandards and Geoanalytical Research*, *32*(3), 247–265. https://doi.org/10.1111/j.1751-908X.2008.00914.x

Rioux, M., Garber, J., Bauer, A., Bowring, S., Searle, M., Kelemen, P., & Hacker, B. (2016). Synchronous formation of the meta-morphic sole and igneous crust of the Semail ophiolite: New constraints on the tectonic evolution during ophiolite formation from high-precision U-Pb zircon geochronology. *Earth and Planetary Science Letters*, *451*, 185–195. https://doi.org/10.1016/j.epsl.2016.06.051

Slama, J., Kosler, J., Condon, D. J., Crowley, J. L., Gerdes, A., Hanchar, J. M., et al. (2008). Plesovice zircon—A new natural reference material for U-Pb and Hf isotopic microanalysis. *Chemical Geology*, *249*(1–2), 1–35. https://doi.org/10.1016/j.chemgeo.2007.11.005

Solari, L. A., Ortega-Gutierrez, F., Elias-Herrera, M., Schaaf, P., Norman, M., de Leon, R. T., et al. (2009). U-Pb zircon geochronology of Palaeozoic units in Western and Central Guatemala: Insights into the tectonic evolution of Middle America. *Origin and Evolution of the Caribbean Plate*, *328*, 295–313. https://doi.org/10.1144/sp328.12

Stacey, J. S., & Kramers, J. D. (1975). Approximation of terrestrial lead isotope evolution by a 2-stage model. *Earth and Planetary Science Letters*, *26*(2), 207–221. https://doi.org/10.1016/0012-821X(75)90088-6

Steiger, R. H., & Jäger, E. (1977). Subcommission on geochronology: Convention on the use of decay constants in geo-and cosmochro-nology. *Earth and Planetary Science Letters*, *36*(3), 359–362. https://doi.org/10.1016/0012-821X(77)90060-7

Wu, F. Y., Yang, Y. H., Xie, L. W., Yang, J. H., & Xu, P. (2006). Hf isotopic compositions of the standard zircons and baddeleyites used in U-Pb geochronology. *Chemical Geology*, *234*(1–2), 105–126. https://doi.org/10.1016/j.chemgeo.2006.05.003

York, D., Evensen, N. M., Martinez, M. L., & Basabe Delgado, J. D. (2004). Unified equations for the slope, intercept, and standard errors of the best straight line. *American Journal of Physics*, *72*(3), 367–375. https://doi.org/10.1119/1.1632486